Large eddy simulation of soot formation in a turbulent lifted flame with a discretised population balance and a reduced kinetic mechanism

Anxiong Liu,[1,2] Binxuan Sun,[3] Tianjie Ding,[3] Stelios Rigopoulos,[3] Kai H. Luo,[4] William P. Jones,[3] and Kun Luo*[2,1]

[1)] *Shanghai Institute for Advanced Study, Zhejiang University, Shanghai 201203, China*
[2)] *College for Energy Engineering, Zhejiang University, Hangzhou, 310027, China*
[3)] *Department of Mechanical Engineering, Imperial College London, London SW7 2AZ, United Kingdom*
[4)] *Department of Mechanical Engineering, University College London, London WC1E 7JE, United Kingdom*

(*Electronic mail: zjulk@zju.edu.cn)

(Dated: 14 July 2024)

This article presents simulations of a turbulent lifted flame using the large eddy simulation (LES)-transport probability density function (*pdf*)- discretised population balance equation (PBE) approach. This approach takes into account the interaction between turbulent reacting flow and soot particle formation. A reduced chemical kinetics mechanism including a series of Polycyclic Aromatic Hydrocarbons (PAHs) species linked to soot formation is generated employing the approach of the Directed Relation Graph Error Propagation (DRGEP), and is tested on a perfectly stirred reactor under varying equivalent ratio conditions and premixed flames. The soot kinetics model includes the PAH-based nucleation and surface condensation, the Hydrogen Abstraction Acetylene Addition (HACA) surface growth and oxidation mechanism, and the size-dependent aggregation. The soot morphology considers the surface area and other geometrical properties for both spherical primary particles and fractal aggregates. The simulation results show, in general, reasonably good agreement with experimental measurements in terms of lifted height, flame shape, flow-field velocity, the hydroxyl radical (OH), and soot volume fraction. A discussion of micromixing and its modelling in the context of the Interaction by Exchange with the Mean (IEM) model is also presented. To investigate the effect of the soot micromixing frequency factor on soot particles, an additional simulation is conducted where this factor is reduced by a factor of 10 for the soot particles. The maximum soot volume fraction is observed to increase slightly. However, compared with the impact of kinetics on soot soot modelling, this effect is a minor one.

I. INTRODUCTION

Soot particles, produced during the combustion of hydrocarbons, can lead to detrimental effects such as deposition on combustor walls or turbine blades, resulting in frictional losses or damage. Furthermore, soot emissions pose a threat to both the atmosphere and human health. With major economies globally endorsing clean energy initiatives, the development of advanced internal combustion engines, gas turbines, and commercial aeroengines that can efficiently control or eliminate soot emissions becomes imperative. Consequently, accurately predicting soot formation in turbulent combustion has emerged as a significant scientific inquiry for engineers and researchers.

This complex issue involves various physical phenomena interacting with one another, including turbulent flow, exothermal chemical reactions, and soot formation. Macroscopic continuum equations, particularly from an Eulerian perspective, are predominantly used as governing equations for engineering applications. Direct Numerical Simulation (DNS) using the Navier-Stokes (NS) equation requires solving an extensive cascade of temporal and spatial scales of turbulent flow down to the Kolmogorov scale, making it virtually impossible for engineering applications. As mean or integral quantities are of primary interest, solving turbulent flows with a turbulence model is not only sufficient but also cost-effective. Two major approaches are Reynolds Averaged Navier-Stokes (RANS) equations, which apply a time average on the NS equation, and Large Eddy Simulation (LES), which applies a spatial filter on the NS equation to remove sub-grid vortices. Reynolds average stress and sub-grid stress, derived in RANS and LES, respectively, share a similar mathematical form but are obtained by treating the momentum equation differently: using time-average or spatial filter, respectively. These unknown terms, representing the effects of turbulence, have to be modelled. Currently, RANS is the most widespread approach in industrial applications, but LES offers increased solution fidelity and potential applicability.

In recent decades, provided that the thermochemical properties and reaction rates are accurate, DNS has shed light on the dynamics of turbulence-chemistry interaction, thereby contributing to the validation of existing turbulent combustion models. From laboratory-scale to industrial-scale, RANS simulations remains widely useful, while LES stands as a very promising technique for turbulent combustion. The Reynolds-average or sub-grid filter operations are also implemented in the transport equations regarding the reactive scalars, resulting in a broad range of unknown quantities for modelling. In RANS, for example, such unknown quantities are the Reynolds-averaged scalar-flux and the mean chemical reaction rates[1]. The Reynolds-averaged / sub-grid scale (*sgs*) scalar fluxes are usually modelled in a way analogous to the Reynolds stress / *sgs* stress and the respective parameters are obtained from experiments or DNS results. Due to the nonlinearity of the Arrhenius law describing the reaction rates, the mean reaction rate would become inaccurate if the routine ap-

proach using the mean temperature and species concentrations was considered. In fact, the majority of turbulent combustion models primarily concern the closure of mean reaction rates. For example, an early model, Bray-Moss-Libby model (BML) for premixed turbulent flame, recovers the mean reaction rates $\overline{\dot{w}_k}$ from the scalar dissipation rate $\overline{\chi}^2$ of the progressive variable c or the flame surface density Σ[3]. Several methods offer solutions for the closure of the mean reaction rate. These include the flamelet model[4–6], CMC (Conditional Moment Closure) method[7–9] and the transported *pdf* approach[10,11], among many others. The last one solves the equations of the joint *pdf* of reactive scalars, instead of the equations of reactive scalars, thus mathematically eliminating the terms of mean reaction rates. A comprehensive review of more methods can be found, for example, in Veynante and Vervisch [1].

Typically, soot is considered as a particulate phase that is polydispersed concerning the particle size. As soot particles are of nanoscale dimensions, they have high Knudsen numbers and behave non-inertially in response to changes in a carrier flow field. Therefore, soot particles in reacting flows are not modelled using multiphase flow schemes. The key physicochemical processes are common to the formation of soot and other kinds of nanoparticles, such as metallic oxides, including nucleation, surface growth, coagulation and aggregation, oxidation and sintering[12,13]. These processes are described by a general population balance equation (PBE)[13–15] which has been widely used in many processes involving polydispersed entities such as aerosols, crystallisation, metallurgy, polymerisation and biochemical processes. Several methods such as moment, discretisation (sectional) and Monte Carlo can be used to solve the PBE, and a review of such methods can be found in the aforementioned references.

The population balance in turbulent flow is unclosed, due to the effect of fluctuations on nonlinear terms such as nucleation, growth and aggregation, in addition to the usual unclosed term associated with turbulent transport[16]. In order to model soot formation in turbulent combustion, therefore, closure is needed to account for these terms. Table I summarises different combinations of methods for turbulence-chemistry-soot particle interaction in various simulation studies in the literature. Sewerin and Rigopoulos [17], Sun and Rigopoulos [18] have proposed the LES-PBE-PDF framework where a discretised PBE (DPBE) is used to describe the soot particle size distribution. This is the approach that will be employed in the present work and has the advantage of having the PBE source term in closed form, although an unclosed term related to micromixing appears.

There are also various physicochemical submodels describing the soot formation processes. For instance, the nucleation rate is linked to C_2H_2[46], benzene[47], large-sized polycyclic aromatic hydrocarbons (PAHs)[48,49] or other hydrocarbon molecules[50]. The dimerisation of PAHs is now commonly accepted for the nucleation modelling, but different PAH molecules are used based on different chemical mechanisms[48,49,51]. For the surface growth rate, simulation studies have used the semi-empirical C_2H_2-based model[46], the HACA (Hydrogen Abstraction Acetylene Addition) model[52], the enhanced-HACA model[49] or the aromatic-site model[53,54]. The morphology of soot is accounted for in different ways, with models ranging in complexity from the spherical particle assumption[55,56], to identical primary particles[57], and polydisperse primary particles[58–60]. The sintering process is only considered by a few simulation studies using the coupled PBE approach (e.g.[59,60]) and Monte Carlo methods (e.g.[61,62].)

In the present paper, we employ the LES-PBE-PDF approach to model the soot formation in turbulent flames together with a comprehensive mechanism that includes detailed gas-phase kinetics including PAH formation[48] and chemistry reduced with the directed relation graph error propagation (DRGEP) approach. The PBE is solved with a recently proposed conservative finite volume method that emphasises accuracy and conservation of moments for the aggregation term[57,63]. With this approach, we simulate a turbulent non-premixed sooting flame, the DLR lifted flame Köhler *et al.* [64,65] and compare our predictions with experimental data. One of the main points of the study is to investigate the modelling of the soot micromixing term and the impact of the micromixing frequency parameter that appears in the modelled PBE-PDF equation.

II. NUMERICAL FRAMEWORK FOR LES-PBE-PDF APPROACH

To investigate the turbulent lifted sooting flame, the discretised PBE approach for modelling the particle size distribution of soot particles, is coupled with the LES-*pdf* approach for turbulent combustion. The implementation of the LES-*pdf* framework is along the same lines as in Jones and Prasad [66]. The details of the LES-PBE-PDF approach are presented in Sewerin and Rigopoulos [17,26,67]. For reference, the main elements of the approach are briefly described below.

A. Equations of species transport and population balance in turbulent reacting flows

For soot formation modelling in turbulent combustion, the gas phase scalars are described by the species transport equations.

$$\frac{\partial \mathbf{Y}}{\partial t} + \frac{\partial (\rho \mathbf{Y})}{\partial x_i} = -\frac{\partial \boldsymbol{J}_i}{\partial x_i} + \boldsymbol{\Omega} \tag{1}$$

where the gas phase reactive scalars $\mathbf{Y}(\boldsymbol{x},t) = [y_1, y_2, \ldots, y_{N_s}, h]^\top$ t are concentrations for each species and the total enthalpy. The mass flux is denoted as $\boldsymbol{J}_i = [j_{1,i}, j_{2,i}, \ldots, j_{N_s,i}, j_{h,i}]$ and the reaction source terms $\boldsymbol{\Omega} = [\omega_1, \omega_2, \ldots, \omega_{N_s}, \omega_h]^\top$ are required to be closed turbulent reaction flows.

In reacting flow at low Mach numbers, the mixture density is often computed in terms of the reactive scalars $\mathbf{Y}(\boldsymbol{x},t)$ based on the ideal-gas law:

$$\rho = \rho\left(\mathbf{Y}(\boldsymbol{x},t)\right) \tag{2}$$

TABLE I. Literature review of the numerical frameworks for modelling soot formation in turbulent flames

Method for turbulence-chemistry-soot interaction	Reference
DNS / HMOM	[19,20] n-heptane (N_2) / Air counterflow non-premixed flame
DNS / MOMIC	[21] n-heptane (N_2) / Air planar jet flame
LES / flamelet / two-moment method	[22] ethanol / heptane jet non-premixed flame
RANS / CMC / two-moment method	[23] CH_4 /air non-premixed flame
RANS / transport PDF / two-moment method	[24] an n-dodecane spray flame (Sandia Spray A)
LES / transport PDF / HMOM	[25] Delft III
LES / transport PDF / DPBE	[17,26] Delft III
RANS / BML flamelet / Monte Carlo	[27] Direct Injection Spark Ignition (DISI)
RANS / Eddy dissipation model (EDM) / two-moment method	[28] CH_4 /air non-premixed flame
LES / flamlet / HMOM	[29] DLR Gas Turbine Combustor
LES / transport PDF / HMOM LES / radiation flamelet & progress variable (RFPV) / HMOM	[30] Delft / Adelaide flame
LES / flamelet / DQMOM	[31] Sandia ethylene/air non-premixed flame
LES / RFPV / HMOM	[32] ethylene-based DLR aircraft Combustor
RANS / flamelet / two-moment method	[33] DLR lifted C_2H_4/air jet non-premixed flame
LES / RFPV / HMOM LES / RFPV / CQMOM	[34] Delft combustor
RANS / flamelet / MOM	[35] DLR lifted C_2H_4/air jet non-premixed flame
RANS / transport PDF / Monte Carlo method	[36] etylene/air jet flames
RANS / EDM / MOM (One moment) RANS / flamelet / MOM (One moment)	[37] CH4–H2/air coaxial jets
RANS / flamelet / MOM	[38] CH_4/air swirl-stabilised non-premixed flame
DNS / CMC / two-moment method	[39] n-heptane spray jet non-premixed flame
RANS / flamelet / two-moment method	[40] C2H4/air jet flame
DNS / Monte Carlo method	[41] n-heptane jet non-premixed flame
RANS / transport PDF / Monte Carlo method	[42] n-dodecane spray flames (ECN Spray A)
RANS / finite-rate chemistry / sectional method	[43] DLR C_2H_4 lifted flame
LES / finite-rate chemistry / sectional method	[44,45] DLR C_2H_4 lifted flame/ DLR pressurised swirlling combustor

The population balance equation describes the evolution of the soot particle size distribution as a result of the transport and aerosol process. A space-dependent distribution is introduced, $n(v,\mathbf{x},t)$, to consider the number density of particles per unit of mixture mass. A discretised form is introduced by applying a sectional method. Here, the continuous function of the particle volume, can be represented by an array of N_p scalar, each of which denotes the number density of particles within a section k of the volume in the range $[v_{k-1}, v_k]$, $k = 1, \cdots, N_\mathrm{p}$. Therefore, the discretised population balance equation is presented,

$$\frac{\partial\left[\rho n_k(\boldsymbol{x},t)\right]}{\partial t} + \frac{\partial\left[\rho u_i n_k(\boldsymbol{x},t)\right]}{\partial x_i} = -\frac{\partial K_{k,i}(\boldsymbol{x},t)}{\partial x_i} + \dot{s}_i(\mathbf{Y},\mathbf{N}) \tag{3}$$

The diffusive flux, $K_{k,i}$ in the sectional volume range $[v_{k-1}, v_k]$,

$$K_{k,i}(\boldsymbol{x},t) = -D_k^\mathrm{p}(\boldsymbol{x},t)\frac{\partial[\rho n_k(\boldsymbol{x},t)]}{\partial x_i} \tag{4}$$

and the finite volume discretisation in the v space of the source term $\dot{s_k}(\mathbf{Y},\mathbf{N})$ is

$$\begin{aligned}\dot{s_k}(\mathbf{Y},\mathbf{N}) =& \underbrace{-\frac{1}{\Delta v_k}\left[\rho n_k \cdot (G(\mathbf{Y},v)+C(\mathbf{Y},v))\right]\Big|_{v_{k-1}}^{v_k}}_{\text{surface growth \& condensation}} \underbrace{+\int_{v_{k-1}}^{v_k} B(\mathbf{Y})\delta(v-v_0)\mathrm{d}v}_{\text{nucleation}} \\ & \underbrace{+\frac{1}{\Delta v_k}\int_{v_{k-1}}^{v_k}\left[\frac{1}{2}\int_0^v \rho^2\beta(w,v-w)n(w,t)n(v-w,t)\mathrm{d}w - \int_0^\infty \rho^2\beta(v,w)n(v,t)n(w,t)\right]}_{\text{coagulation source \& death}}\end{aligned} \tag{5}$$

A conservative discretisation method with respect to the coagulation process was proposed in Liu and Rigopoulos[57]. For the surface growth and condensation, which is a convective term in the volume space, with a total variation diminishing (TVD) scheme is employed[68].

B. LES / Eulerian *pdf* method

Our in-house code BOFFIN-LES is adpoted to study the turbulent lifted sooting flame. In this present pressure-based compressible LES scheme, the sub-grid stress tensor $\tau_{ij}^{\rm sgs} = \overline{\rho}(\widetilde{u_i u_j} - \widetilde{u}_i\widetilde{u}_j)$ is formulated with the standard Smagorinsky model:

$$\tau_{ij}^{\rm sgs} = 2\mu^{\rm sgs}\widetilde{S_{ij}} \tag{6a}$$

$$\mu^{\rm sgs} = \overline{\rho}(C_{\rm s}\Delta)^2(2\widetilde{S_{ij}}\widetilde{S_{ij}})^{\frac{1}{2}} \tag{6b}$$

$$\widetilde{S_{ij}} = \frac{1}{2}\left(\frac{\partial \tilde{u_j}}{\partial x_i} + \frac{\partial \tilde{u_i}}{\partial x_j}\right) \tag{6c}$$

where the $\widetilde{\ }$ operator denotes the density-weighted Favre-averaging. Due to difficulties encountered in evaluating the filtered values of the chemical source terms in the species transport equations and population balance equations, a joint filtered *pdf* of reactive and particle number scalars is employed. An exact equation describing the evolution of the joint *pdf* can be derived by standard methods, *e.g.* Gao and O'Brien [69], and Brauner, Jones, and Marquis [70] added the resolved part of the convection and the molecular mixing to both sides of the equation so that the modelled form of the joint *pdf* equation becomes:

$$\frac{\partial\left[\overline{\rho}\widetilde{P(\boldsymbol{\Psi})}\right]}{\partial t} + \frac{\partial\left[\overline{\rho}\tilde{u}_i\widetilde{P(\boldsymbol{\Psi})}\right]}{\partial x_i} = \underbrace{-\frac{\partial}{\partial\psi_\alpha}\left[\overline{\rho}\dot{\omega}_\alpha(\boldsymbol{\Psi})\widetilde{P(\boldsymbol{\Psi})}\right]}_{\text{I.reaction}} \underbrace{-\frac{\partial}{\partial x_i}\left[\overline{\rho u_i P(\boldsymbol{\Psi})} - \overline{\rho}\tilde{u}_i\widetilde{P(\boldsymbol{\Psi})}\right]}_{\text{II.}sgs-\text{convection}} \underbrace{-\frac{\partial}{\partial x_i}\left[\Gamma\frac{\partial\widetilde{P(\boldsymbol{\Psi})}}{\partial x_i}\right]}_{\text{III.molecular diffusion}}$$
$$\underbrace{-\sum_{\alpha=1}^{N_{\rm s}+N_{\rm p}+1}\sum_{\beta=1}^{N_{\rm s}+N_{\rm p}+1}\frac{\partial^2}{\partial\psi_\alpha\partial\psi_\beta}\left[\left(\Gamma\overline{\frac{\partial y_\alpha}{\partial x_i}\frac{\partial y_\beta}{\partial x_i}\,|\,\mathbf{Y}=\boldsymbol{\Psi}}\right)\widetilde{P(\boldsymbol{\Psi})}\right]}_{\text{IV.micromixing}\quad \mathscr{M}(\boldsymbol{\Psi};\boldsymbol{x},t)} \tag{7}$$

where the fine-grained joint probability density function (PDF) of reactive scalars $P(\boldsymbol{\Psi};\boldsymbol{x},t)$ is set the *delta* functions for the convenience of mathematical transformation.

$$P(\boldsymbol{\Psi};\boldsymbol{x},t) = \delta\left[\boldsymbol{\Psi} - \begin{pmatrix}\mathbf{Y}(\boldsymbol{x},t)\\ \mathbf{N}(\boldsymbol{x},t)\end{pmatrix}\right] = \prod_{\alpha=1}^{N_{\rm s}+N_{\rm p}+1}\delta\left[\psi_\alpha - y_\alpha(\boldsymbol{x},t)\right] \tag{8}$$

where $\boldsymbol{\Psi} = [\psi_1,\psi_2,\ldots,\psi_{N_{\rm s}},\psi_{N_{\rm s}+1},\ldots,\psi_{N_{\rm s}+N_{\rm p}+1}]^\top$ is the composition domain of the scalar array $\mathbf{Y}(\boldsymbol{x},t)$ and $\mathbf{N}(\boldsymbol{x},t)$.

In Eq. 7, term I represents the chemical reaction term, which now appears in a closed form and does not require any modelling. Term II represents the residual convection term at the *sgs* level, which is analogous to the *sgs* stress tensor in Eq. 6, modelled as

$$\overline{\rho u_i P(\boldsymbol{\Psi})} - \overline{\rho}\tilde{u}_i\widetilde{P(\boldsymbol{\Psi})} = -\Gamma^{\rm sgs}\frac{\partial\widetilde{P(\boldsymbol{\Psi})}}{\partial x_i} \tag{9}$$

with a consistent form with term III, the molecular diffusion of the *pdf*. Term IV $\mathscr{M}(\boldsymbol{\Psi};\boldsymbol{x},t)$ demonstrates a filtered conditional pattern of 'scalar dissipation rate' and can be explained as a *sgs* micromixing. In this research, the Interaction by Exchange with the Mean (IEM) model was proposed by Villermaux and Devillon [71], Dopazo and O'Brien [72], Dopazo [73].

$$\mathscr{M}(\boldsymbol{\Psi};\boldsymbol{x},t) = \frac{\overline{\rho}}{2\tau^{\rm sgs}}\sum_{\alpha=1}^{N_{\rm s}+N_{\rm p}+1}\frac{\partial}{\partial\psi_\alpha}\left[\left(\psi_\alpha - \widetilde{y_\alpha(\boldsymbol{x},t)}\right)\widetilde{P(\boldsymbol{\Psi})}\right] \tag{10}$$

where $\tau^{\rm sgs}$ is the *sgs* mixing time scale, and its inverse, the *sgs* mixing frequency is given by Jones and Prasad [66]

$$\frac{1}{\tau^{\rm sgs}} = C_{\rm D}\frac{\mu+\mu^{\rm sgs}}{\overline{\rho}\Delta^2} \tag{11}$$

and the *sgs* micromixing constant $C_{\rm D} = 2.0$ follows the previous applications of LES-transport *sgs* on turbulent flames, *.i.e.*[66,74].

The equation describing the evolution of the *pdf* (Eq. 7) is solved using the Eulerian stochastic field method. $P(\boldsymbol{\Psi})$ is represented by an ensemble of M stochastic fields for each of the $N_{\rm s}+1$ scalars $\boldsymbol{\zeta}^m(\boldsymbol{x},t) = [\zeta_1^m,\ldots,\zeta_{N_{\rm s}+N_{\rm p}+1}^m], m = 1,\ldots M$. Now, substitute the stochastic samples for the *pdf* in the transport *pdf* equations (Eq. 7). After some algebraic manipulation (see Valiño [75]) and identifying the drift and diffusion coefficient of *Ito sde*[76]. The final differential equation is

$$\begin{aligned}\overline{\rho}\mathrm{d}\zeta_\alpha^m = &-\overline{\rho}\tilde{u}_i\frac{\partial\zeta_\alpha^m}{\partial x_i}\mathrm{d}t + \frac{\partial}{\partial x_i}\left[(\Gamma+\Gamma^{\rm sgs})\frac{\partial\zeta_\alpha^m}{\partial x_i}\right]\mathrm{d}t\\ &+\overline{\rho}\frac{\sqrt{2(\Gamma+\Gamma^{\rm sgs})}}{\overline{\rho}}\frac{\partial\zeta_\alpha^m}{\partial x_i}\mathrm{d}W_i^m\\ &-\frac{\overline{\rho}}{2\tau_{\rm sgs}}\left(\zeta_\alpha^m - \tilde{\phi}_\alpha\right)\mathrm{d}t + \overline{\rho}\dot{\omega}_\alpha(\zeta^m)\mathrm{d}t\end{aligned} \tag{12}$$

where $\mathrm{d}W_i^m$ represents increments of a (vector) Wiener process, different for each stochastic field but independent of the spatial location $\boldsymbol{x}$.

III. CHEMICAL KINETICS, SOOT MECHANISM AND THE COMPUTATIONAL SETUP

A. Chemical kinetics reduction using DRGEP

The original chemical reactions are adopted from Ref.[48] and comprise a total of 148 species and 928 reactions. This mechanism, developed based on the GRI 3.0 mechanism, including the chemistry of soot precursors such as acetylene, different isomers of C_3H_4 isomers, and benzenel. It encompasses all major pathways of PAHs formation up to pyrene ($C_{16}H_{10}$) and cyclopentapyrene ($C_{18}H_{10}$). Extensive validation of this mechanism has been performed for the combustion of various fuels, ranging from methane to iso-octane and one-ring aromatics, across different configurations such as homogeneous auto-ignition, laminar premixed flames and diffusion flames. This mechanism has been used in modelling inception and growth of soot in laminar ethylene diffusion flames[77]. Thermodynamic properties of the species are obtained from the sources presented in Blanquart, Pepiot-Desjardins, and Pitsch [48]. In the case of turbulent flames, consistent molecular mass diffusivity is considered instead of differential diffusion. The Schmidt number, Sc, is assumed to have a value of 0.7, and is utilised for both the molecular mass diffusivity Γ and the *sgs* mass diffusivity Γ^{sgs}.

$$\Gamma = \frac{\mu}{\mathrm{Sc}} \tag{13a}$$

$$\Gamma^{\mathrm{sgs}} = \frac{\mu^{\mathrm{sgs}}}{\mathrm{Sc}} \tag{13b}$$

However, the real-time computation of the complete chemical kinetics at each spatial grid node, time step and stochastic field is prohibitively expensive in the turbulent combustion simulation employing the *pdf* approach. To address this issue, the aforementioned mechanism is reduced using the directed relation graph error propagation (DRGEP) method to decrease the computational load. In order to gather data samples for DRGEP analysis, an ensemble of perfectly stirred reactor (PSR) simulations were performed with varying initial temperatures, equivalence ratios and pressure. For each collected data sample, the interaction coefficient of each species to the target species were calculated, which indicates the contribution of the selected species to the production/consumption of the target species, and then the coefficients were averaged over all collected samples. In this work, major species (*e*.g. C_2H_4,H_2O, CO and CO_2) and species related to soot formation, including PAHs species in the nucleation and condensation processes, gas chemical species used in the HACA mechanism (see Section III B) are selected as the target species. Species with small interaction coefficients to the target species are removed from the mechanism. More details of the DRGEP method can be found in Refs[78,79]. The size of the original chemical kinetics has been reduced by around 1/3. The simplified kinetics includes 101 species and 652 steps of chemical reactions. The reduced mechanism was tested on PSR (perfectly stirred reactor) with those obtained using complete mechanism (shown in Fig. 1), with two equivalence ratio conditions, namely $\phi = 1.0$, 5.0 and two initial temperature conditions, $T = 1400\,\mathrm{K}$ and $1800\,\mathrm{K}$. The results show that both the profiles of temperature, major species and minor PAH species in the DRGEP condensed mechanism are in excellent agreement with the complete mechanism. Note that these species are all linked to soot formation modelling. The only discrepancy is that species A_2 are overpredicted by approximately 10% when the initial temperature is $1800\,\mathrm{K}$ and in lean combustion conditions ($\phi = 0.5$ and 1.0). Another test case is on 1D laminar premixed flame with two equivalence ratio conditions $\phi = 1.0$ and 1.4 (shown in Fig. 2 of the supplementary materials). The profiles of temperature, major species and minor PAH species are accurately predicted by the DRGEP mechanism. Therefore, the validated DRGEP condensed mechanism will be applied in the following soot formation simulations.

B. Soot formation mechanism

The processes of soot formation involve the nucleation, surface growth, condensation and coagulation of spherical particles and fractal aggregates. The model for soot nucleation and condensation in this work are referenced from Blanquart and Pitsch [80]. In this model, the self-collision of two PAHs forms a dimer, which is an intermediate state between the gaseous PAHs and the particulate soot. The dimers are then consumed either by self-coalescence to form soot nuclei or by condensation onto the surface of soot particles. Eight types of PAHs for dimerisation, from naphthalene ($C_{10}H_8$) up to cyclopenta[cd]pyrene ($C_{18}H_{10}$), are listed in the Table II. The self-collision rate, $\omega_{\mathrm{PAH},i}$ is given by the following expression:

$$\omega_{\mathrm{PAH},i} = \gamma_i \sqrt{\frac{4\pi R_{\mathrm{J}} T}{M_i}} d_{\mathrm{PAH},i}^2 [\mathrm{PAH}]_i^2 N_{\mathrm{A}}^2 \tag{14}$$

where N_{A} denotes Avogadro's number, R_{J} is the gas constant (unit $[\mathrm{kmol}\cdot\mathrm{K/kJ}]$) and M_i is the molar mass of PAH_i. d_i indicates the mean diameter of the molecules PAH_i.

Assume that the consumption of dimers by the nucleation and condensation sub-processes and the production of dimers are in a quasi-steady state, resulting in a quadratic equation

$$a_{\mathrm{nuc}}[\mathrm{dimer}]^2 + b_{\mathrm{cond}}[\mathrm{dimer}] = \sum_{l=1}^{8} \omega_{\mathrm{PAH},i} \tag{15}$$

The positive root of Eq. 15 is accepted as the concentration of dimers. The coefficients a_{nuc} and b_{cond} are determined by the nucleation and condensation rates, respectively. The nucleation rate, w_{nuc}, takes the following form,

$$w_{\mathrm{nuc}} = E_F \left(\frac{3}{4\pi}\right)^{\frac{1}{6}} \sqrt{\frac{6k_{\mathrm{B}}T}{\rho_{\mathrm{s}}}} 4\sqrt{2} v_{\mathrm{dimer}}^{\frac{1}{6}} [\mathrm{dimer}]^2 N_{\mathrm{A}}^2 \tag{16}$$

where $E_F = 2.2$ is the Van der Waals factor[81] and $\rho_s = 1800\,\mathrm{kg/m^3}$ is the density of soot particle. An average volume of dimers v_{dimer} is used to represent the different volume of dimers produced by the self-collision of the eight PAHs.

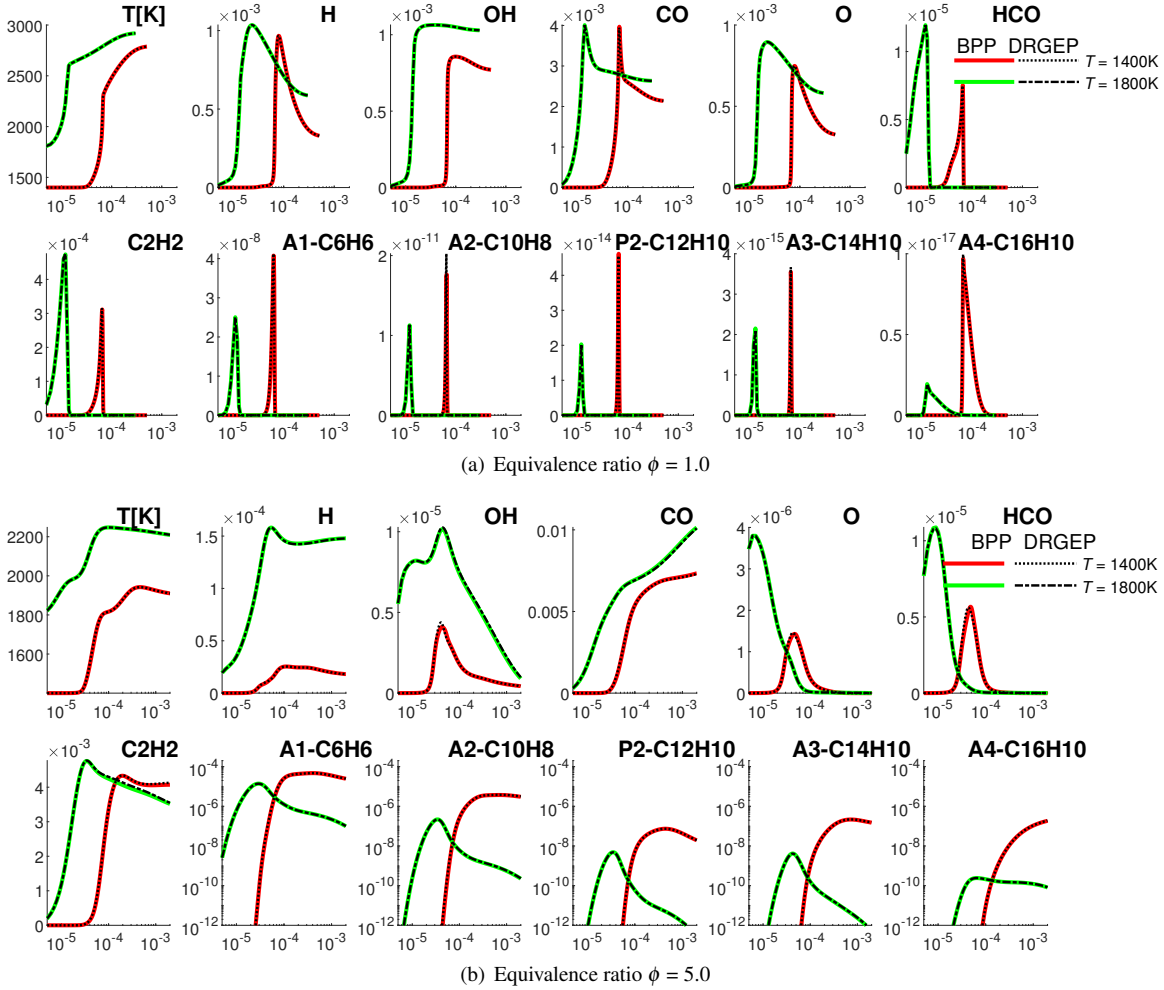

(a) Equivalence ratio $\phi = 1.0$

(b) Equivalence ratio $\phi = 5.0$

FIG. 1. Application of the DRGEP reduced mechanism to the 0D perfectly stirred reactor

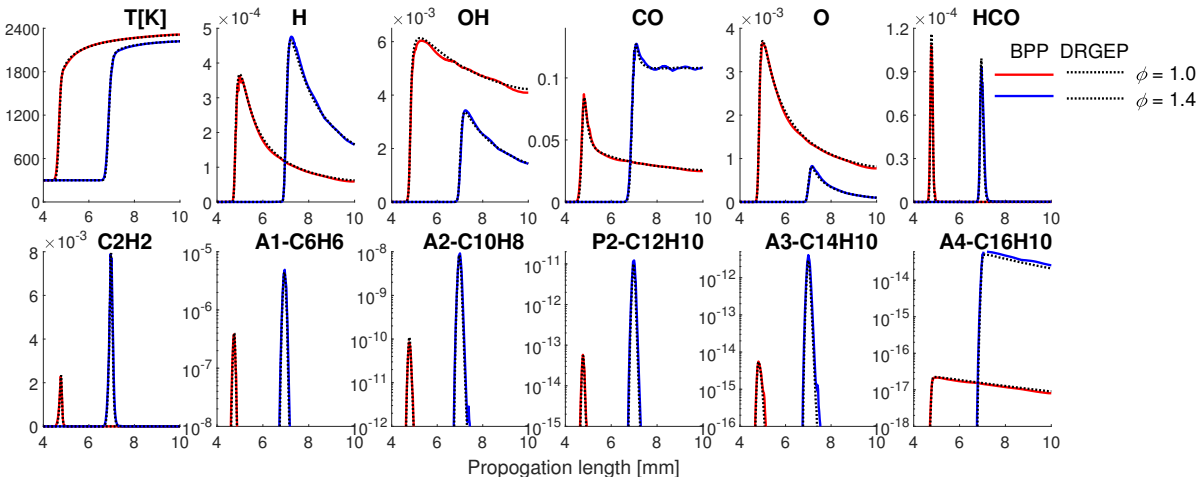

FIG. 2. Application of the DRGEP reduced mechanism to the 1D laminar premixed flame

Species	Molar mass M_i [kg/kmol]	Name	Collision efficiency γ_i
$C_{10}H_8$	128.17	Naphthalene	0.0010
$C_{12}H_8$	152.20	Acenaphthylene	0.0030
$C_{12}H_{10}$	154.21	Biphenyl	0.0085
$C_{14}H_{10}$	178.24	Phenathrene	0.0150
$C_{16}H_{10}$	202.26	Pyrene	0.0250
		Acephenanthrylene	0.0250
		Fluoranthene	0.0250
$C_{18}H_{10}$	226.28	Cyclo[cd]pyrene	0.0390

TABLE II. List of PAH species of dimerisation for the nucleation and surface condensation sub-processes

Thus, the nucleation source term in Eq. 5 is written as

$$\dot{B} = w_{\text{nuc}} \frac{2v_{\text{dimer}}}{v_0 \Delta v_0} \tag{17}$$

indicating that two dimers are coalesced to form a soot nucleus and Δv_0 is the interval covers the volume of nuclei. The condensation rate is modelled as,

$$C(\mathbf{Y}, v) = \beta_{\text{dimer},v} N_{\text{A}} [\text{dimer}] \cdot v_{\text{dimer}} \tag{18}$$

Therefore, the coefficients a_{nuc} and b_{cond} in Eq. 15 are determined as

$$a_{\text{nuc}} = \frac{2w_{\text{nuc}}}{[\text{dimer}]^2} \tag{19a}$$

$$b_{\text{cond}} = \beta_{\text{dimer},v} N_{\text{A}} \tag{19b}$$

Soot surface growth and oxidation are modelled via the H-abstraction/C_2H_2 addition (HACA) mechanism, originally proposed by Frenklach and Wang[82]. The reaction rates are calculated based on the parameters of Table 2 and 3 in Ref.[80]. In the HACA mechanism, a hydrogen atom is abstracted from the C-H bond (C_{soot}-H) and the C_2H_2 molecule is added to an active site ($C_{\text{soot}}\cdot$). The number density of (C_{soot}-H) is estimated to be $\chi_{\text{soot}} = 2.3 \times 10^{15} \text{sites/cm}^2$, based on the diameter of a benzene ring and the distance between PAH layers of soot particles[82]. The concept of surface reactivity was introduced with the parameter α, which is the main uncertainty in the HACA mechanism. Constant values were proposed in early research, but later it was considered to be dependent on the local temperature[83,84], particle size[85,86] or the residence time[87,88]. In this work, the α value is taken from the soot formation modelling for Santoro flames[77].

$$\alpha = 0.0037 \exp\left(\frac{9000}{T}\right) \tag{20}$$

The net surface growth rate (including oxidation) is calculated as follows,

$$G(v, \mathbf{Y}) = \frac{A_{\text{s}}(v)}{\rho_{\text{s}}} \dot{R}(\text{HACA}), \tag{21}$$

where $\dot{R}(\text{HACA})$ represent the surface-specific soot growth rate, which is a function of α, χ_{soot}, the reaction rates associate with the HACA mechanism[80]. $A_{\text{s}}(v)$ is the volume-dependent surface area of a soot particle.

The collision kernel β for the coagulation and aggregation sub-processes takes different forms depending on the Knudsen number $\text{Kn} = 2\lambda_f/d$, where λ is the gas mean free path and d is the particle diameter. Three regimes are identified, namely the free molecule regime ($\text{Kn} < 0.1$), the continumm regime ($\text{Kn} > 10$) and the transition regime ($0.1 < \text{Kn} < 10$), with the expressions below, respectively,

$$\beta^{\text{fm}}(v_i, v_j) = 2.2 \sqrt{\frac{\pi k_{\text{B}} T}{\rho_{\text{s}}(v_i + v_j)}} \left(d(v_i) + d(v_j)\right)^2, \tag{22a}$$

$$\beta^{\text{c}}(v_i, v_j) = \frac{2k_{\text{B}}T}{3\mu} \left(\frac{\text{Cu}(v_i)}{d(v_i)} + \frac{\text{Cu}(v_j)}{d(v_j)}\right) \left(d(v_i) + d(v_j)\right), \tag{22b}$$

$$\beta^{\text{tr}}(v_i, v_j) = \frac{\beta^{\text{fm}}(v_i, v_j)\beta^{\text{c}}(v_i, v_j)}{\beta^{\text{fm}}(v_i, v_j) + \beta^{\text{c}}(v_i, v_j)}. \tag{22c}$$

where the Cunningham slip correction factor $\text{Cu}(v) = 1 + 1.257\text{Kn}_v$ and $d(v)$ represents either the spherical particle diameter or the collision diameter of an aggregate. The fractional dimension $D_{\text{f}} = 1.8$ and the fractal prefactor $k_{\text{f}} = 1.94$ for all aggregates in this work.

The description of soot morphology is detailed in Liu *et al.*[77]. This study refers to morphological parameters, including the surface area $A_{\text{s}}(v)$, the diameter of gyration $d_{\text{g}}(v)$ and the hydrodynamic diameter $d_{\text{h}}(v)$), concerning primary soot particles and fractal-like aggregates. Based on experimental data, soot particles are modelled as spherical nanoparticles if their size is smaller than 30.8 nm in diameter. For larger sizes, soot particles are considered to be fractal aggregates composed of primary particles with a diameter of 30.8 nm. This soot model and parameters are the same as in the studies of[77] in ethylene laminar co-flow flames and III in the Sandia turbulent flame[18]).

Due to the significant difference in size between soot particles and gaseous molecules, the molecular diffusivity of soot particles is excluded from consideration. In the context of turbulent flames, a consistent molecular mass diffusivity is considered rather than differential diffusion. The Schmidt number Sc, is assumed to have a value of 0.7, and it is utilised for both the molecular mass diffusivity Γ and the *sgs* mass diffusivity Γ_{sgs}.

IV. FLAME CONFIGURATION AND COMPUTATIONAL SETUP

The flame to be simulated is the DLR lifted ethylene jet flame[64,65]. The fuel burner consists of a circular nozzle with an inner diameter of 2.0 mm. The co-annular dry air is supplied through a contoured nozzle that converges from an inner diameter of 280 mm to 140mm over a vertical distance of 310 mm. The air flow rate is flows is 320 g/min, providing a homogeneous co-flow of oxidiser. To shield the flame from laboratory-induced air currents, the burner is mounted within an optically accessible casing. Ethylene at room temperature, 295 K, is injected centrally through a tube with a bulk velocity V_{fuel} of 44 m/s, corresponding to a flow rate of 10.4 g/min. The jet-exit Reynolds number is thus 10000 and the resulting flame is lifted and exhibits a visible flame length of 400-500 mm. The experiment was conducted at atmospheric pressure.

The computational domain is a rectangular parallelepiped with dimensions of 600 mm, 220 mm and 220 mm in the axial-x direction, as well as the y and z directions, respectively. The domain is discretised into a grid with 260, 145, and 145 volume cells in the x, y, and z directions, respectively. The grid is stretched by a factor of 1.013 axially to enhance resolution near the burner. Radially, 12 cells are allocated within the inner burner region to capture the fuel jet with a high resolution of 0.1 mm, while the grid is progressively stretched with factors ranging from 1.05-1.10 towards the lateral boundaries. At the inflow boundaries, the mean axial velocity of the jet fuel is prescribed with power-law profiles using an exponent of 1/6. The co-flow air is set with a constant axial inflow velocity. The turbulence intensities for all flows are specified as 6%. For the fuel jet, the root mean square (RMS) inflow velocity varies quadratically: it reaches four times the nominal centreline value at the jet rim and remains constant along the co-flow. The lateral boundaries are treated using an entrainment/outflow condition with zero gradient for the velocity and scalars. At the exit plane, a convective outflow condition is applied to the velocity field, while the scalar fields are subjected to a condition of zero gradient. Previous studies on the eulerian stochastic-*pdf* method have shown that the use of eight stochastic fields is adequate for achieving convergence of the means and RMS values of the reactive scalars. In accordance, eight fields are employed in this work. The grid sensitivity analysis is also conducted by refining the mesh with a doubled volume cell number. Information of the coarse and fine grid mesh is displayed in Table III. A comparison between the simulation results showing using the original and refined mesh is presented in the profiles of axial velocity, temperature and soot volume fraction (see Figs. 4(a), 5 and 8) in Section V, proving the consistency of predicted results along the flame centreline between the coarse and fine meshes. Therefore, the simulation results with the original mesh are presented and analysed in other results figures in Section V.

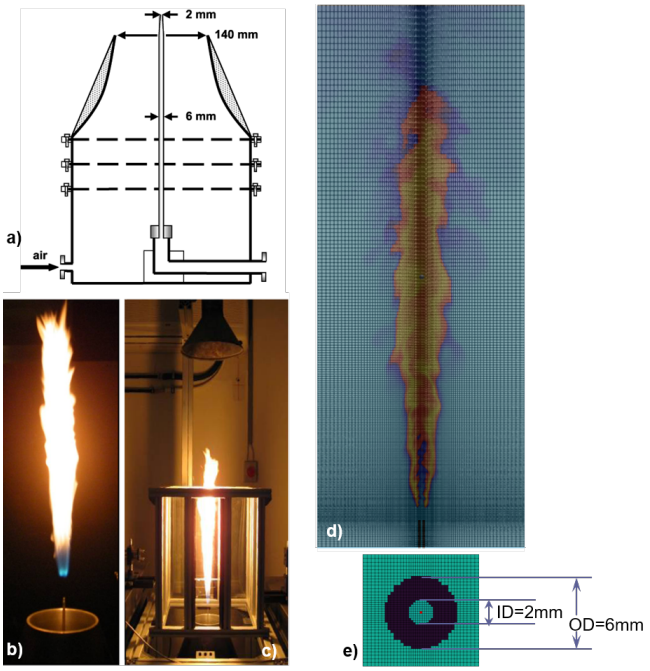

FIG. 3. Photographs of the turbulent lifted jet flame and the grid of the computational domain: (a)The burner schematic; (b) a snapshot of the lifted jet flame; (c) jet burner in optical housing for defined boundary conditions; (d) the grid in a cut plane through the centreline; (e) the grid for the burner. Image (a- c) from[64] with permission from Springer Nature

V. RESULTS AND DISCUSSION

A. Simulation prediction of the flame shape, temperature statistics and soot formation

Figure 4 compares the calculated temperature profiles with experimental results. The mean axial velocity profiles obtained from the simulation and the experimental measurements show excellent agreement along the flame centreline, as depicted in Fig. 4(a). Figure 4(b) presents the comparison of radial profiles of the mean axial velocities at four different heights as well as the RMS of velocities at the three of those heights. The LES simulation resutls of the mean axial velocities match well the PIV data, except for a slight underprediction at distances greater than 10 mm away from the centreline at the downstream height of 363 mm. The LES simulation also show excellent agreement in predicting the velocity RMS, except for a slight underprediction by approximately half in the flame centre region at a height of 213 mm. The LES simulation results also show good agreement in the velocity RMS prediction except the underprediction by half in the flame centre region at the height 213 mm. This is likely due to the stronger turbulent dissipation at downstream region.

Figure 5 compares the present LES simulation work with the CARS (Coherent Anti-Stokes Raman Scattering)) measurement for the axial profiles of the mean and RMS temperature along the flame centreline. It should be noted that our LES simulation overpredicts the mean centreline temper-

Mesh	Domain name	Domain size (length × width × height)	Total element No.	Element No. in Domain F
Coarse	Domain C	$110 \times 110 \times 600\,\mathrm{mm}^3$	$145 \times 145 \times 260$	$137 \times 137 \times 248 = 4{,}465{,}000$
Fine	Domain F	$88 \times 88 \times 550\,\mathrm{mm}^3$	$165 \times 165 \times 325$	$165 \times 165 \times 325 = 8{,}848{,}000$

TABLE III. Information of domain size and element number for the coarse and fine grid mesh

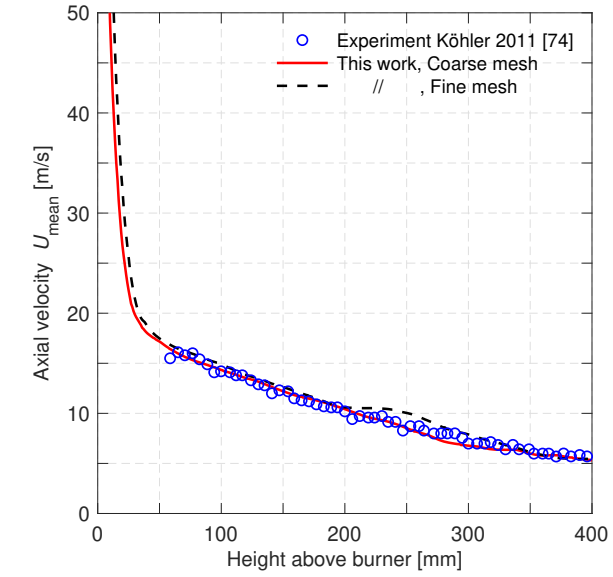

(a) Axial profile along the flame centreline

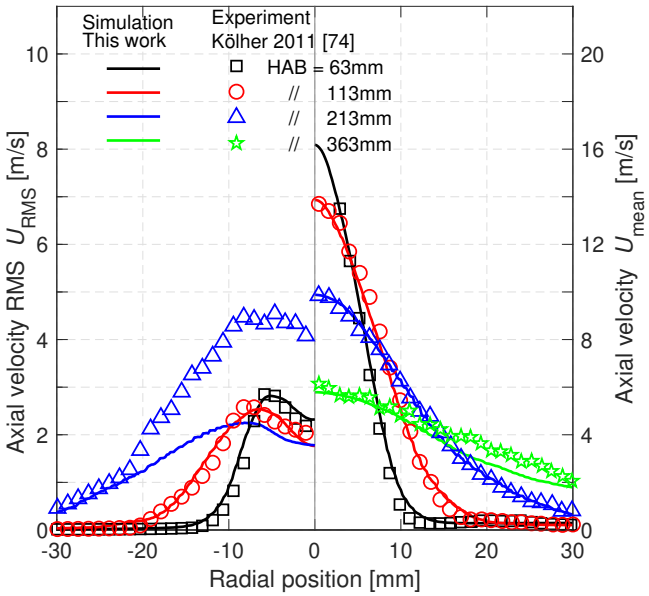

(b) Radial profiles for selected heights: RMS (left) and mean (right)

FIG. 4. Comparison of the simulated and measured profiles of the mean axial velocities: the simulation results are compared from the experimental PIV data and the RANS simulation results by Köhler *et al.* [43]

ature, with a maximum difference of 300 K up to a height of 250 mm HAB. On the other hand, the LES simulation shows good agreement with the CARS measurement for the temperature RMS profile, except for a significant underprediction observed between 90-160 mm HAB. It is noticeable that simulations conducted on the both coarse and fine meshes exhibit a consistent overprediction of temperature on the flame centreline prior to 250 mm HAB above the burner.

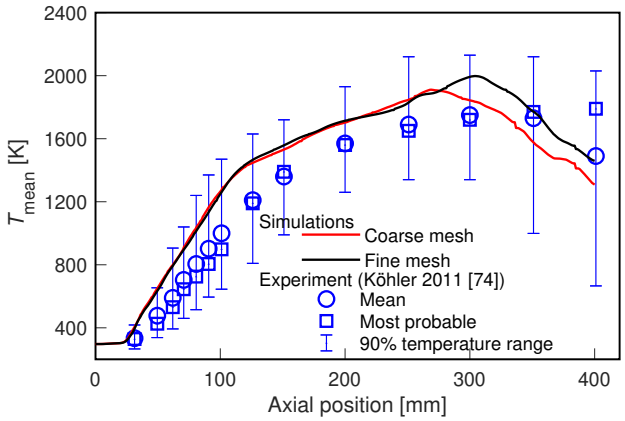

(a) Time-averaged temperature

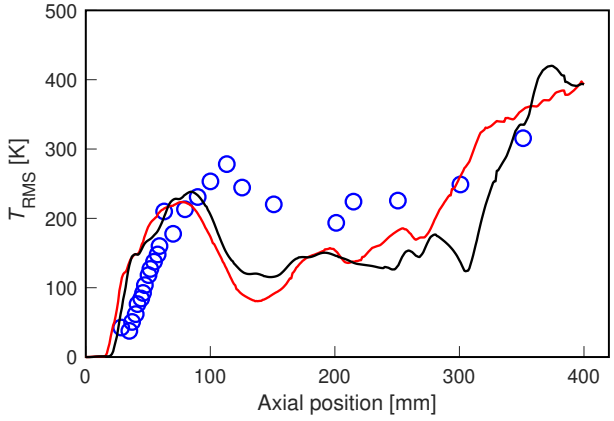

(b) RMS of temperature

FIG. 5. Axial profiles of temperature on the flame centreline

Figure 6 provides a more detailed comparison of the predicted radial temperature profiles for different heights, with the nTLAF measurements by Köhler *et al.* [64] and Gu *et al.* [89] Note that the nTLAF measurement datasets from different references show some discrepancy, such as the maximum temperature difference of 400 K of T_{mean} at 213 mm HAB and the discrepancy of radial positions for peak temperatures. The

simulated and experimental maximum mean temperatures at 63 mm HAB are located at the wings of the flame, but further downstream the temperature difference between the centreline and wings of the flame decreases, until at 310 mm HAB, the two wings merge and the maximum temperatures are on the centreline. Consistent with the prediction on the flame centreline (Fig. 5), our LES simulation also overpredicts the mean temperature around the flame centreline at each height. However, for hot regions (5-10 mm away from the flame centreline), the LES simulation performs more accurately. Therefore, we may conclude that the heat release in the flame front regions is adequately captured. Additionally, the overprediction of mean temperature along the flame centreline suggests enhanced thermal diffusion, which can be attributed to the stronger turbulent mixing in our prediction. Regarding the temperature RMS profiles, our LES simulation aggres well with Köhler's measurements[64], except for an underprediction at 113 mm HAB. However, at 310 mm HAB, our LES simulation underpredicts the measured temperature RMS profile[89] by approximately half.

Figure 7 compares the radial profiles of the predicted normalised OH mole fractions with the normalised intensity signals obtained from OH-planar laser-induced fluorescence (OH-PLIF) measurements[64], using the respective maximum values of the entire field. It should be noted that OH-PLIF measurements exhibit slight asymmetries and a radial shift, resulting in scattered points from two wings that do not form smooth profiles. From the mean normalised OH profiles, two notable strengths of our LES simulation emerge. Firstly, the predicted peak normalised OH values match well with the OH-PLIF measurements at all selected heights. Secondly, the radial positions of the peak OH values demonstrate better agreement with the measurements, particularly at heights of 113 mm, 160 mm, and 213 mm HAB. It is interesting to note that our work reveals a lack of alignment between the radial positions of peak OH mole fraction and those of peak temperature. In diffusion flames, the peak OH zone is known to occur in the flame front, where the temperature is lower than the maximum. The maximum temperature, in turn, can occur closer to or further away from the fuel source, depending on various factors such as the specific fuel and oxidiser mixture, flow rate, and flame geometry. Additionally, shape and magnitude of RMS profiles agree well between the simulation and measurements, providing confidence in the predicted flame shape.

Figure 8 compares our LES simulations in terms of the mean and RMS of soot volume fraction along the flame centreline with the laser-induced incandescence (LII) measurements. One important finding is that, despite the significant disparity in temperature (see Figure 6), the two experimental sources show substantial agreement in terms of mean soot volume fraction (Figure 8(a)). We performed our LES simulations with two different soot micromixing frequency factors $\kappa = 1.0$ and $\kappa = 0.1$, these factors slightly affect soot prediction. One main drawback of our simulations is that they predict soot formation starting too early in the flame, with peaks occurring prior to the measured location at 294 mm. However, our LES simulation with a soot micromixing frequency factor of $\kappa = 0.1$ does accurately predict the peak soot volume fraction, which matches the measured value of 0.5 pmm and is larger than the cases with $\kappa = 1.0$. For the calculated RMS profiles of the soot volume fraction in Fig. 8(b), our LES simulation underpredicts the RMS especially in the upstream region.

In addition, we also present the mean and RMS of the soot volume fraction along the flame centreline obtained from the LES-PBE-PDF simulations using different meshes and different soot micromixing frequencies in Fig. 8. The simulation conducted on the fine mesh achieves a similar peak magnitude of soot volume fraction, which aligns well with the experiment measurement. Simulations using different meshes also predict an earlier onset of soot formation, with the peak soot volume fraction occurring 50 - 60 mm upstream of the measured data. However, in the refined mesh, the change in the soot volume fraction by adjusting the soot micromixing frequency is less significant. This can be attributed to the fact, with a finer mesh, the importance of micromixing term decreases.

Figure 9 illustrates the radial profiles of soot volume fraction for five heights, comparing to LII measurements. Both LII datasets exhibit the same trend of a narrow two-peak radial distribution of f_v at a height of113 mm. As the flame progresses downstream, this distribution broadens and becomes a one-peak profile with the maximum value on the centreline. The present LES simulation roughly reproduces this trend. Note that Gu's LII dataset has a narrower f_v than Köhler's measurement, and our LES simulation agrees well with Gu's LII data in shape and magnitude from 113-263 mm. The transition from a two-peak to a single-peak profile is also visible in the measured f_v-RMS and is confirmed by both LES sources. Similar to the centreline profile (see Fig. 8(b)), our LES simulation underpredicts the radial RMS values and also exhibits a narrower RMS distribution downstream.

Figure 10 compares the simulated primary particle size, D_p, at the flame centreline and radial profiles at three different heights, with experimental data provided by Köhler *et al.* [64] and Gu *et al.* [89]. The simulated results consistently show an overprediction of 30% - 50% in the primary particle size compared to the experimental measurements.

Figure 11 (a-b) show the contours of instantaneous and time-averaged temperature from the simulation. The temperature fields exhibit a sharp gradient at a height of approximately 20 mm, which is also consistent with the lift-off-height defined by half of the maximum OH mole fraction (refer to Fig. 11(d-e)). This finding aligns well with the lift-off height of 22.3 ± 1.5 mm in the experimental results of Köhler *et al.* [43]. The statistics were derived from 500 OH chemiluminescence images, defining the position of half of the maximum OH-PLIF intensity as the the lifted height, representing the steep gradient of OH concentration. A RANS simulation by Köhler *et al.* [43] revealed that ignition occurred at the lift-off height of approximately 25 mm. Accurately predicting the lift-off height in turbulent flames is a highly challenging task due to the intricate interplay between turbulent diffusion and chemistry.

Figure 11(c-n) present contours of the instantaneous, time-

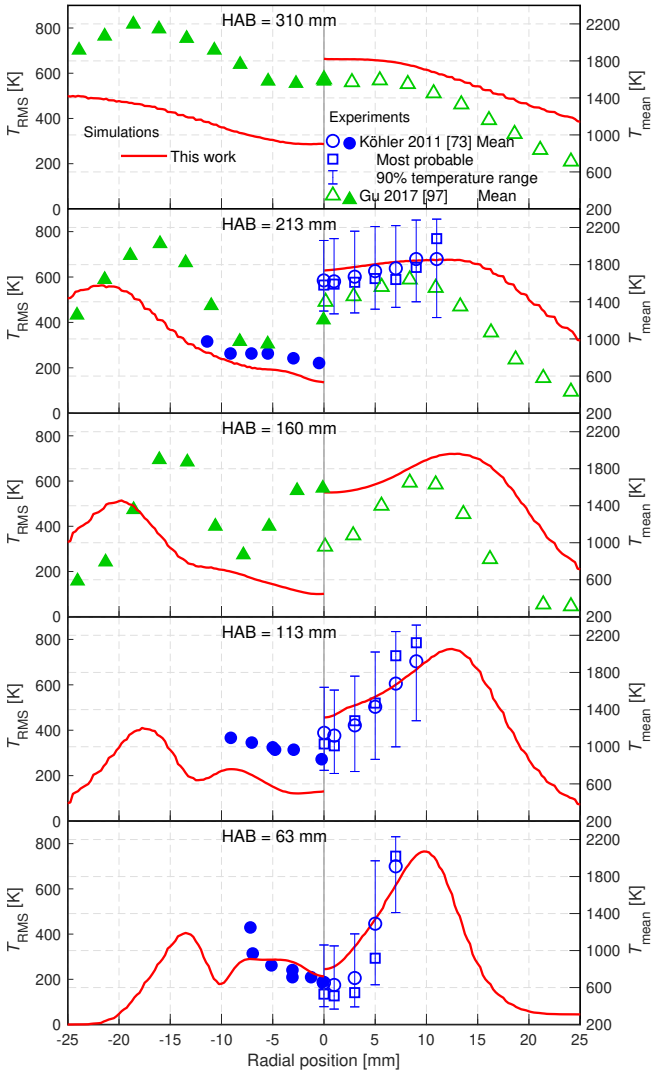

FIG. 6. Radial profiles of temperature for selected heights: RMS (left); mean (right)

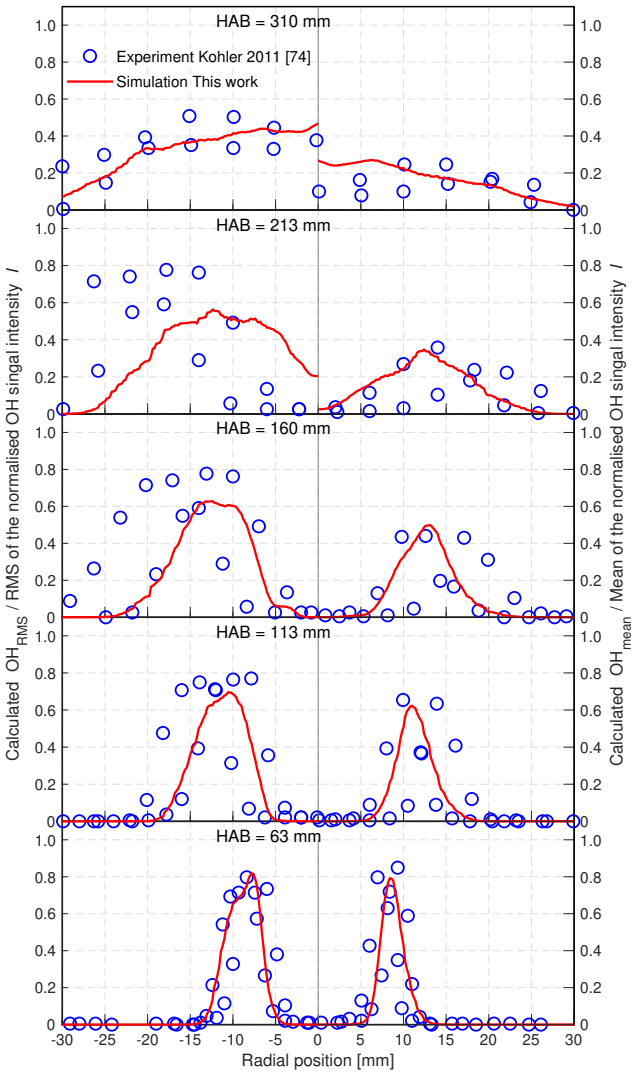

FIG. 7. Radial profiles of normalised OH mole fraction with normalised OH-PLIF signal intensity for selected heights: RMS (left); mean (right)

averaged and root-mean-square (RMS) of soot volume fraction, as well as the mole fraction of OH, A2 (naphthalene) & A3 (phenanthrene), A4 (pyrene) species from the simulation. These contours are compared with matching signals obtained from laser diagnostic measurements, such as OH-PLIF, LII and PAH-PLIF[43,64], shown in Fig. 11(o-w). Same properties from the simulation and optical measurements are aligned in the same column of Fig. 11. The modelling results of the OH mole fraction show a high level of consistency with the OH-PLIF measurements, as demonstrated by contour plots of the instantaneous shot, RMS, and time-averaged values in Fig. 11(c-e) and (o-q). The only notable difference is that the averaged OH mole fraction exhibits a wider distribution downstream in the flame compared to the OH-PLIF measurements. The OH radical is often considered as an intermediate species in combustion for visualising the flame front, as it is formed in the reaction zone and rapidly converted at lower temperature.

The instantaneous concentration mappings of soot volume fraction predicted by the simulation (Fig. 11(c)) show a smaller and narrower shape and distribution than the random collage of the LII measurement (Fig. 11(r)). The LII signals visualises the emergence of soot particles from 50 mm HAB and their extension towards the upper region of the flame. The optical image also demonstrates the swirling dynamic motions of the vortices and the breakup into secondary scales. In contrast, the RMS and averaged contours of soot volume fraction (Fig. 11(g-h)) show more positive aspects, despite still exhibiting narrower distributions than the optical measurements. These contours emerge from 55-60 mm HAB and extends downstream toward the upper region. The predicted positions of the RMS maxima are consistent with the LII measurement, while the maximum averaged values are predicted to be approximately 50 mm upstream. The absolute range of

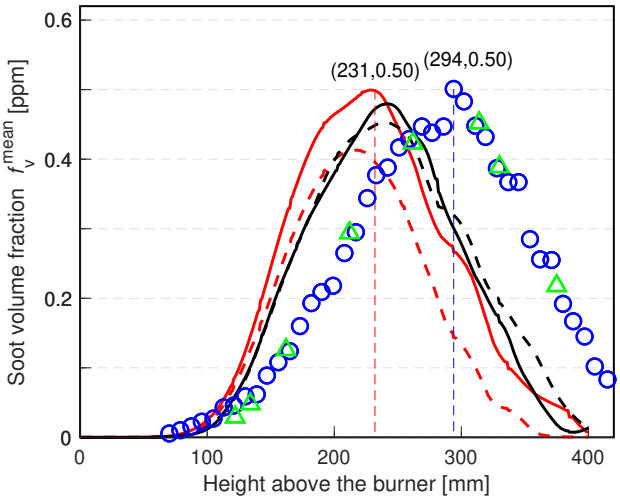

(a) Mean

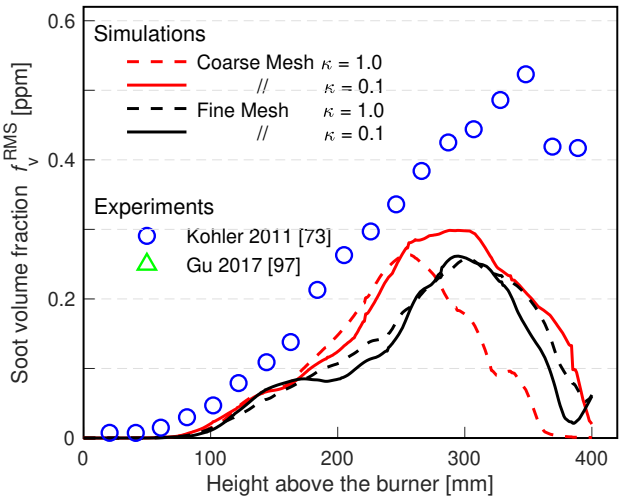

(b) RMS

FIG. 8. Comparison of the simulated and measured profile of the soot volume fraction on the flame centreline. Simulations with the coarse and fine mesh are compared, showing the effect of adjusting the soot micromixing frequency

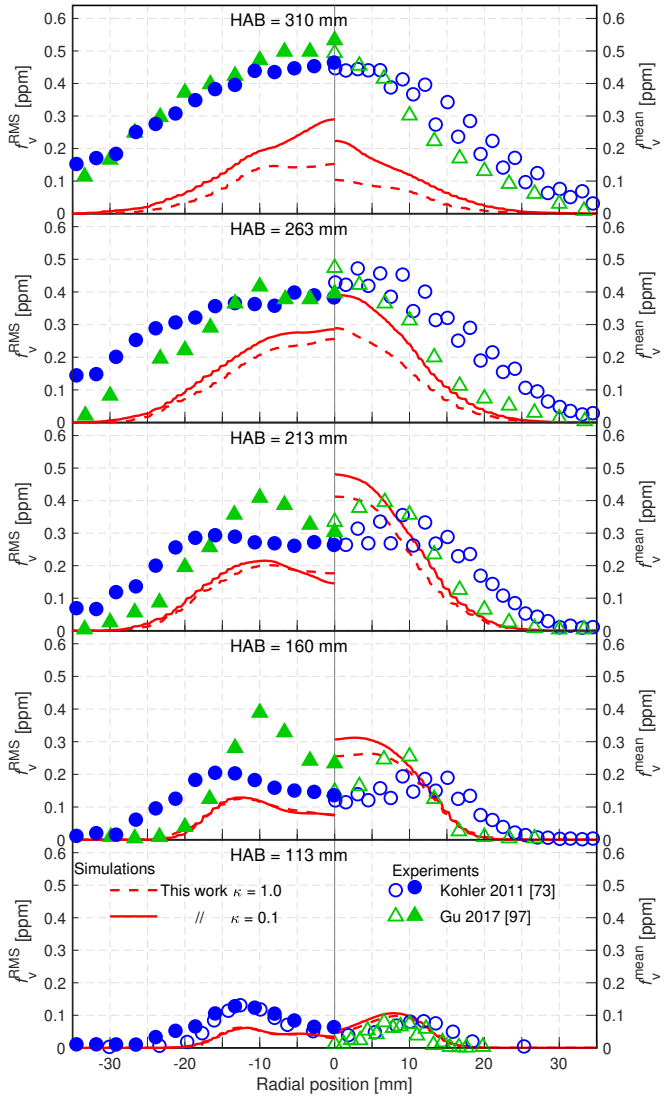

FIG. 9. Comparison of the simulated and measured radial profiles of the soot volume fraction for selected heights: RMS (left) and mean (right).

the averaged soot volume fraction matches that of the LII measurement.

PAHs are recognised as important soot precursors, as they contain fused aromatic rings that form the building blocks of soot. In the PAH-PLIF measurements[43] (Fig. 11(u-w)), a detection filter bandpass of 305-325 nm was chosen to include PAH species with the carbon number estimated to be between 10-14, like naphthalene (A2, $C_{10}H_8$) and phenanthrene (A3, $C_{14}H_{10}$). However, the modelled contour plots of A2 and A3 (Fig. 11(i-k)) do not match the PAH-PLIF signals because the PAH-PLIF signals emerge from 20-30 mm HAB and extends downwards into the upper range of the flame, while the predicted A2 & A3 mole fraction disappear at around 300 mm HAB. In contrast, the modelled mole fraction contours of pyrene (A4, $C_{16}H_{10}$) drawn in Fig. 11(l-m) show better consistency with the PAH-PLIF signals, as the A4 species still exists at the flame top. In general, the PAH-PLIF signals overlap with the LII (soot volume fraction) signals in the measurement, and the soot volume fraction contours are spatially consistent with the distribution of A4 species rather than A2 & A3 species in the simulation. In fact, the concentrations of A2 & A3 is around 100 times larger than the A4 species, contributing significantly to the production of soot dimers in the nucleation process occurring at the early stage of the flame. However, the increase in soot volume fraction is primarily due to the particle surface growth process, in which the hydrocarbon species (C_2H_2) is absorbed onto the surface of nascent soot particles. Therefore, contours of soot volume fraction should be downstream than the A2 & A3 mole fraction distribution.

Figure 12 illustrates the profiles of the nucleation, surface growth and condensation processes at the centreline and two selected heights. The centreline profile reveals that the nucleation rate dominates the soot formation process, with a over-

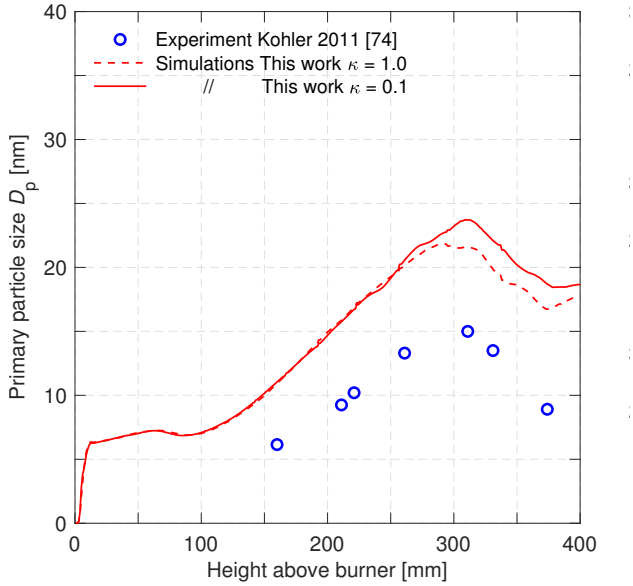

(a) Centreline

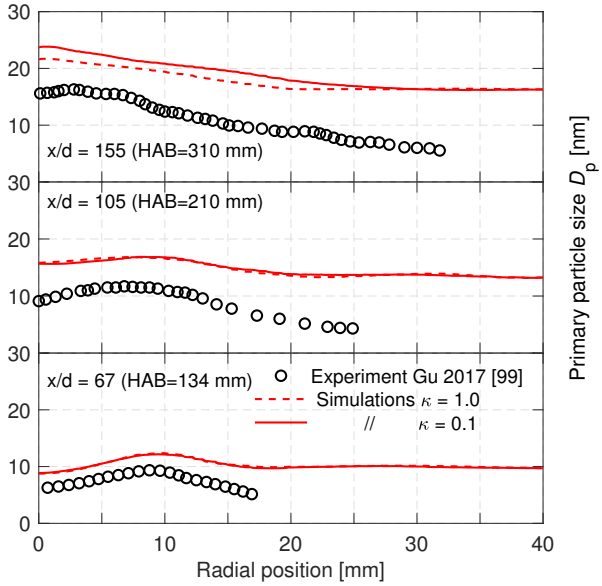

(b) Radial profiles at different heights

FIG. 10. Simulated primary particle size on the flame centreline and different heights

whelming contribution than the condensation process and the surface growth process [unit: $m^3(soot)/m^3(mixture)\cdots$] in the early stage (HAB < 220 mm). As the micromixing correction factor decreases from 1.0 to 0.1 in the peak-value region (125 - 175 mm HAB), both the nucleation rate and condensation rate increase, resulting in enlarged soot formation. The surface growth process becomes the dominant contributor to soot volume fraction from 220 - 260 mm HAB, although its peak value is considerably smaller than the nucleation process. Subsequently, the oxidation process plays a major role in reducing soot. However, no evident effect of the micromixing frequency factor is observed on the surface growth and oxidation processes in the downstream region.

B. Discussion on the modelling of the micromixing term in the LES-PBE-PDF equation

The results shown so far have demonstrated the effect of the micromixing timescale, which is the most important unclosed parameter in the LES-PBE-PDF formulation with the IEM model. Changing it by an order of magnitude had a relatively small effect on the results. In addition, by refining the mesh and adjusting the soot micromixing frequency, the variation in the soot volume fraction becomes less significant. In this section, we provide some further comments on the physical reasons behind this effect.

In high Reynolds and Peclet number turbulent flows, the scalar interfaces will be stretched and distorted by the energetic turbulent motions, down to scales comparable to the Batchelor length scales. At these scales, the scalar gradients and interfacial area will be sufficiently large for significant diffusive mixing to occur. In these circumstances, consistent with Batchelor - Kolmogorov - Oboukhov arguments[90–93], the scalar diffusive mixing rate will be dominated by the rate at which the scalar is transported across the inertial-convective subrange, which can be parametrised by the resolved motions and their timescales. This description is widely used but relies on an underlying assumption of local isotropy. However, recent DNS evidence[94,95] on small-scale passive scalar statistics at high Schmidt numbers indicates that they deviate from those of velocity and are not isotropic. The consequence of this on the characterisation of scalar mixing at high Schmidt numbers is unknown. In the absence of any further information, we have adopted the IEM model. While this has some known deficiencies related to the the evolution of *pdf* shape, this does not seem to have a dominant influence in LES. The model involves the resolved time scale ν_{sgs}/Δ^2 consistent with the mixing description above. Given the basis of the IEM model, it is difficult (if not impossible) to justify trying to account for the low diffusivities of soot particles by modifying the mixing time scale. If high Schmidt number scalar transport is found to have a direct effect on the mixing model and consequently one-point scalar statistics, then new modelling is required.

The direct numerical simulation of high-Schmidt number flows in principle could provide modelling information but this requires resolving scales smaller than the Kolmogorov scale, down to the Batchelor length scale. The length scale of the latter is related to that of the Kolmogorov scale, η, as $\eta_c = \eta\sqrt{Sc}$ so that, for e.g. Schmidt number = 1000, η_c is $\sqrt{1000}$ times smaller than the Kolmogorov scale; thus 31^3 = 29,791 times more cells are required to resolve η_c. While some studies of transport at high Sc have appeared[96–101], mainly on passive and inert scalars, such simulations are beyond the capability of present-day computing power for reacting flows and soot.

Most importantly, the uncertainties in the kinetic parameters (most notably the surface reactivity) are certainly of a higher order than the effect of micromixing. Establishing a

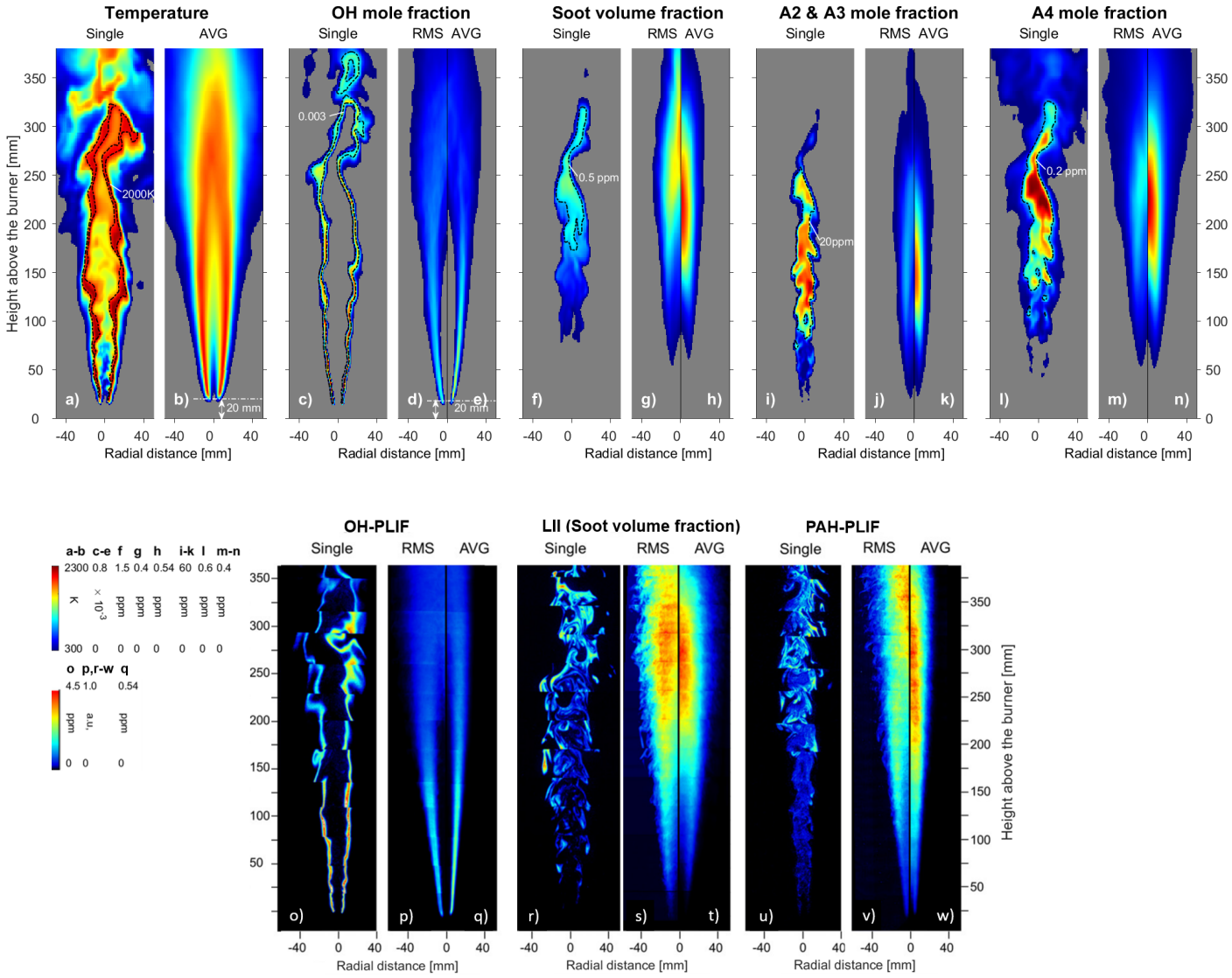

FIG. 11. Contour plots (a- n) compare the instantaneous, time-averaged and root-mean-square (RMS) values of the flame and soot properties in this simulation, with laser diagnostic images (o-w) from[43] with permission from Elsevier) in a cut plane through the centreline: (a) Instantaneous temperature with (b) the corresponding time averaged plots. (c) Instantaneous OH mole fraction with (d) the corresponding RMS and (e) averaged plots. (f) Instantaneous soot volume fraction with (j) the corresponding RMS and (k) averaged plots. (i) Instantaneous naphthalene (A2) & phenanthrene (A3) (pyrene) mole fraction with (j) the corresponding RMS and (k) averaged plots. (l) Instantaneous pyrene (A4) mole fraction with (m) the corresponding RMS and (n) averaged plots. (o) Instantaneous OH-PLIF image representing the OH distribution with (p) corresponding RMS and (q) averaged 2D-PLIF images. (r) Instantaneous LII image representing the soot distribution with (s) corresponding RMS and (t) averaged 2D-LII images. (u) Instantaneous PAH-LII images with (v) corresponding RMS and (w) averaged 2D-PLIF images. The contour plots in the same column positions show the same properties from both the simulation and experimental measurements, respectively. The legend on the right bottom displays the scales of the contours.

firm basis in the kinetics of soot formation should therefore be considered a higher priority, before the issues related to particle micromixing can be properly evaluated.

VI. CONCLUSIONS

In this article, we applied the LES-PBE-PDF approach, together with the stochastic field method, to model the evolution of soot formation. This method provides closure for the unclosed terms arising from the interaction of turbulence, chemistry and soot formation processes, although unclosed terms

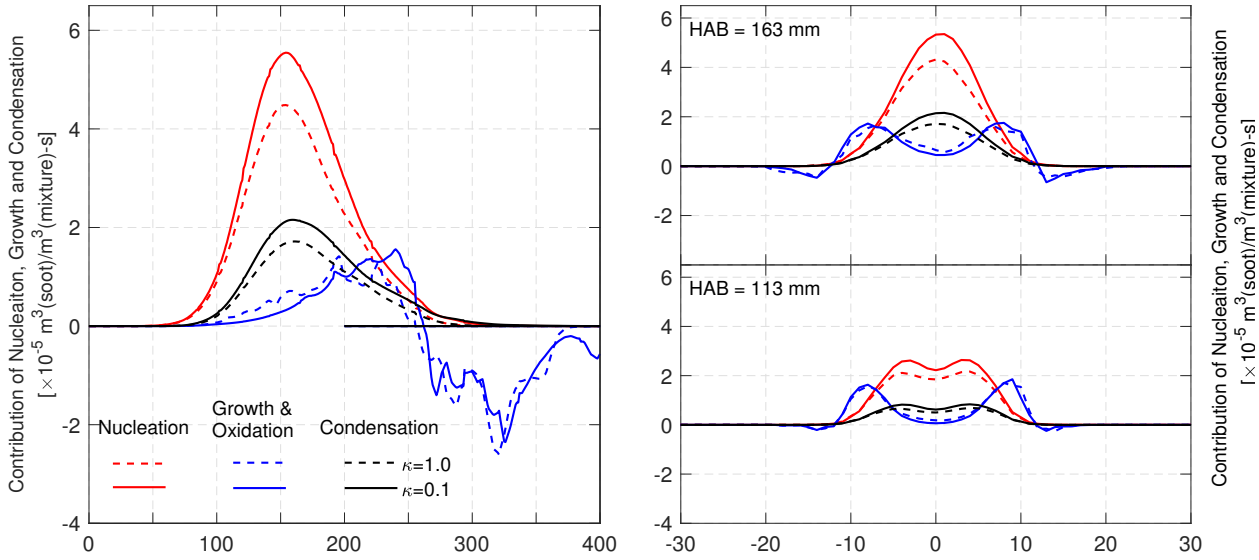

FIG. 12. Contour plots of the time-averaged contributions of processes of nucleation, surface growth (oxidation) and condensation with varying soot micromixing frequency factor.

remain, most notably the micromixing term. To reduce the computational load of reactive scalars, the detailed chemical mechanism of 149 species developed by Blanquart, Pepiot-Desjardins, and Pitsch [48] has been condensed into 104 species with a series of PAHs remaining via the DRGEP (direct relation graph error propagation) approach and the level of chemical detail is still impressive. The reduced mechanism has been validated by data from the zero-dimensional perfectly stirred reactor and has shown good agreement with the original complete mechanism at different equivalent ratios, particularly in terms of temperature profiles, major species and the minor PAHs species linked to soot formation. The soot kinetics model includes the PAH-based nucleation and surface condensation, the HACA surface growth and oxidation mechanism, and the size-dependent aggregation. The soot morphology estimates the surface area and other geometrical properties differently for spherical primary particles and fractal aggregates.

The modelling results show, in general, reasonably good agreement with experimental measurements from the DLR turbulent lifted flame. The lift-off height, flame shape and flow-field velocity are correctly predicted. The temperature on the centreline is overpredicted by 100 – 300 K below 150 mm HAB, but well predicted on the flame wings with peak temperatures. The spatial distribution of OH species, the soot volume fraction and the concentration of pyrene correspond reasonably well to the OH-PLIF, LII signal and PAH-PLIF signals. Regarding the spatial distribution of soot volume fraction, soot is predicted to occur and disappear earlier in the upstream and downstream regions of the flame. However, better results are attained with respect to the magnitude of soot volume fraction. The present LES simulation also exhibits good predictions of the RMS values, including those of the velocity, temperature, OH species and soot volume fraction.

In the framework of the LES-PBE-PDF approach, the micromixing term for soot properties was modelled with the IEM model, initially by using the same timescale as for gas-phase species and subsequently by decreasing the soot micromixing frequency by 1/10. In the latter case, the soot volume fraction only increases by a little. The value of the soot micromixing frequency parameter was discussed in light of turbulence theory and the assumptions inherent in the IEM model. The effect of changing this parameter is considerably smaller than the present uncertainties in soot kinetics, hence establishing a basis in kinetics should be considered a priority before this issue can be properly evaluated.

ACKNOWLEDGEMENTS

Funding for the research by the National Natural Science Foundation of China under Grant Nos. 52206177 and 51925603, and Shanghai Pujiang Program under Grant No. 22PJ142800 is gratefully acknowledged.

[1] D. Veynante and L. Vervisch, "Turbulent combustion modeling," Progress in Energy and Combustion Science **28**, 193–266 (2002).
[2] T. Mantel and R. Borghi, "A new model of premixed wrinkled flame propagation based on a scalar dissipation equation," Combustion and Flame **96**, 443–457 (1994).
[3] K. Bray, M. Champion, and P. Libby, "The interaction between turbulence and chemistry in premixed turbulent flames," in *Turbulent Reactive Flows*, edited by R. BorghiS and N. Murthy (Springer, New York, 1989) pp. 541–563.
[4] N. Peter, "Laminar flamelet concepts in turbulent combustion," International Symposium on Combustion **21**, 1231–1250 (1988).
[5] J. Duclos, D. Veynante, and T. Poinsot, "A comparison of flamelet models for premixed turbulent combustion," Combustion and Flame **95**, 101–117 (1993).
[6] Z. Chen, I. Langella, R. Barlow, and N. Swaminathan, "Prediction of local extinctions in piloted jet flames with inhomogeneous inlets using unstrained flamelets," Combustion and Flame **212**, 415–432 (2020).

[7] A. Klimenko and R. Bilger, "Conditional moment closure for turbulent combustion," Progress in Energy and Combustion Science **25**, 595–687 (1999).

[8] P. Siwaborworn and A. Kronenburg, "Conservative implementation of les-cmc for turbulent jet flames," High Performance Computing in Science and Engineering **12**, 159–173 (2013).

[9] A. Kronenburg and T. Stein, "A comparison of flamelet models for premixed turbulent combustion," Flow, Turbulent, Combustion **98**, 803–816 (2017).

[10] S. Pope, "PDF methods for turbulent reactive flows," Progress in Energy and Combustion Science **11**, 119–192 (1985).

[11] G. Bulat, W. Jones, and A. Marquis, "No and co formation in an industrial gas-turbine combustion chamber using les with the eulerian sub-grid pdf method," Combustion and Flame **161**, 1804–1825 (2014).

[12] M. Kholghy, M. Saffaripour, C. Yip, and M. Thomson, "The evolution of soot morphology in a laminar coflow diffusion flame of a surrogate for jet A-1," Combustion and Flame **160**, 2119–2130 (2013).

[13] V. Raman and R. Fox, "Modeling of fine-particle formation in turbulent flames," Annual Review of Fluid Mechanism **48**, 159–190 (2016).

[14] D. Ramkrishna, *Population Balances: Theory and Applications to Particulate Systems in Engineering* (Academic Press, 2000).

[15] S. Rigopoulos, *Population Balance of Particles in Flows: from Aerosols to Crystallisation* (Cambridge University Press, 2024).

[16] S. Rigopoulos, "PDF method for population balance in turbulent reactive flow," Chemical Engineering Science **62**, 6865–6878 (2007).

[17] F. Sewerin and S. Rigopoulos, "Algorithmic aspects of the les-pbe-pdf method for modeling soot particle size distributions in turbulent flames," Combustion Science and Technology **191**, 766–796 (2019).

[18] B. Sun and S. Rigopoulos, "Modelling of soot formation and aggregation in turbulent flows with the les-pbe-pdf approach and a conservative sectional method," Combustion and Flame **242**, 112152 (2022).

[19] F. Bisetti, G. Blanquart, M. E. Mueller, and H. Pitsch, "On the formation and early evolution of soot in turbulent nonpremixed flames," Combustion and Flame **159**, 317–335 (2012).

[20] A. Attili, F. Bisetii, M. Mueller, and H. Pitsch, "Damkohler number effects on soot formationand growth in turbulent nonpremixed flames," Proceedings of the Combustion Institute **35**, 1215–1223 (2015).

[21] F. Bisetti, A. Attili, and H. Pitsch, "Advancing predictive models for particulate formation in turbulent flames via massively parallel direct numerical simulations," Philosophical Transactions of the Royal Society A: Mathematical, Physical and Engineering Sciences **372**, 20130324 (2014).

[22] A. Yuen, G. Yeoh, V. Timchenko, T. Chen, Q. Chan, C. Wang, and D. Li, "Comparison of detailed soot formation models for sooty and non-sooty flames in an under-ventilated iso room," International Journal of Heat and Mass Transfer **115**, 717–729 (2017).

[23] A. Kronenburg, R. Bilger, and J. Kent, "Modelling soot formation in turbulent methane–air jet diffusion flames," Combustion and Flame **121**, 24–40 (2000).

[24] M. chishty, M. Bolla, E. Hawkes, and Y. Pei, "Soot formation modelling for n -dodecane sprays using the transported pdf model," Combustion and Flame **192**, 101–109 (2018).

[25] P. Donde, V. Raman, M. Mueller, and H. Pitsch, "LES/PDF based modeling of soot–turbulence interactions in turbulent flames," Proceedings of the Combustion Institute **34**, 1183–1192 (2013).

[26] F. Sewerin and S. Rigopoulos, "An LES-PBE-PDF approach for predicting the soot particle size distribution in turbulent flames," Combustion and Flame **189**, 62–76 (2018).

[27] J. Etheridge, S. Mosbach, M. Kraft, H. Wu, and N. Collings, "Modelling soot formation in a DISI engine," Proceedings of the Combustion Institute **33**, 3159–3167 (2011).

[28] K. Saqr, H. Aly, M. Sies, and M. Wahid, "Effect of free stream turbulence on NOx and soot formation in turbulent diffusion CH4-air flames," International Communications in Heat and Mass Transfer **37**, 611–617 (2010).

[29] H. Koo, M. Hassanaly, V. Raman, M. Muller, and K. Geigle, "Large-eddy simulation of soot formation in a model gas turbine combustor," Journal of Engineering for Gas Turbines and Power **139**, 031503 (2017).

[30] W. Han, V. Raman, M. E. Mueller, and Z. Chen, "Effects of combustion models on soot formation and evolution in turbulent nonpremixed flames," Proceedings of the Combustion Institute **37**, 985–992 (2019).

[31] Y. Xuan and G. Blanquart, "Effects of aromatic chemistry-turbulence interactionson soot formation in a turbulent non-premixed flame," Proceedings of the Combustion Institute **35**, 1911–1919 (2015).

[32] S. Chong, M. Hassanaly, H. Koo, M. Muller, V. Raman, and K.-P. Geigle, "Large eddy simulation of pressure and dilution-jet effects on soot formation in a model aircraft swirl combustor," Combustion and Flame **192**, 452–472 (2018).

[33] M. Yen, V. Magi, and J. Abraham, "Modeling soot formation in turbulent jet flames at atmospheric and high-pressure conditions," Energy & Fuel **32**, 8857–8867 (2018).

[34] S. Chong, V. Raman, M. Mueller, P. Selvaraj, and H. Im, "Effect of soot model, moment method, and chemical kinetics on soot formation in a model aircraft combustor," Proceedings of the Combustion Institute **37**, 1065–1074 (2019).

[35] R. Saini and A. De, "Assessment of soot formation models in lifted ethylene/air turbulent diffusion flame," Thermal Science and Engineering Progress **49-61**, 3 (2017).

[36] R. Mehta, D. Haworth, and M. Modest, "Composition PDF/photon monte carlo modeling of moderately sooting turbulent jet flames," Combustion and Flame **157**, 982–994 (2010).

[37] S. Chouaieb, W. Kriaa, H. Mhiri, and P. Bournot, "Presumed PDF modeling of microjet assisted CH4–H2/air turbulent flames," Energy Conversion and Management **120**, 412–421 (2016).

[38] L. Wang, S. Chatterjee, Q. An, A. Steinberg, and Ö. L. Gölder, "Soot formation and flame structure in swirl-stabilized turbulent non-premixed methane combustion," Combustion and Flame **209**, 303–312 (2019).

[39] M. Bolla, D. Farrace, Y. Wright, K. Boulouchos, and E. Mastorako, "Influence of turbulence–chemistry interaction for n-heptane spray combustion under diesel engine conditions with emphasis on soot formation and oxidation," Combustion and Flame **18**, 330–360 (2014).

[40] M. Busupally and A. De, "Numerical modeling of soot formation in a turbulent C2H4/air diffusion flame," International Journal of Spray and Combustion Dynamics **8**, 67–85 (2014).

[41] M. Lucchesi, A. Abdelgadir, A. Attili, and F. Bisetti, "Simulation and analysis of the soot particle size distribution in a turbulent nonpremixed flame," Combustion and Flame **178**, 35–45 (2017).

[42] S. Fernandez, C. Paul, A. Sircar, A. Imren, D. Haworth, and S. Roy, "Soot and spectral radiation modeling for high-pressure turbulent spray flames," Combustion and Flame **190**, 402–415 (2018).

[43] M. Köhler, K. Geigle, T. Blacha, P. Gerlinger, and W. Meier, "Experimental characterization and numerical simulation of a sooting lifted turbulent jet diffusion flame," Combustion and Flame **159**, 2620–2635 (2012).

[44] M. Grader, C. Eberle, and P. Gerlinger, "Large-eddy simulation and analysis of a sooting lifted turbulent jet flame," Combustion and Flame **215**, 458–470 (2020).

[45] M. Grader and P. Gerlinger, "Influence of operating conditions on flow field dynamics and soot formation in an aero-engine model combustor," Combustion and Flame **258**, 112712 (2023).

[46] K. Leung, R. Lindstedt, and W. Jones, "A simplified reaction mechanism for soot formation in nonpremixed flames," Combustion and Flame **87**, 289–305 (1991).

[47] R. Lindstedt, "Simplified soot nucleation and surface growth steps for nonpremixed flames," in *Soot Formation in Combustion*, edited by H. Bockhorn (Springer-Verlag, 1994) p. 417–441.

[48] G. Blanquart, P. Pepiot-Desjardins, and H. Pitsch, "Chemical mechanism for high temperature combustion of engine relevant fuels with emphasis on soot precursors," Combustion and Flame **156**, 588–607 (2009).

[49] Y. Wang and S. Chung, "Soot modeling of counterflow diffusion flames of ethylene-based binary mixture fuels," Combustion and Flame **162**, 586–596 (2015).

[50] R. Hall, M. Smooke, and M. Colket, "Predictions of soot dynamics in opposed jet diffusion flames," in *Physical and Chemical Aspects of Combustion: A Tribute to Irvin Glassman, Combustion Science and Technology Book Series*, Vol. 4, edited by F. Dryer and R. Sawyer (Gordon and Breach, 1997) p. 189–229.

[51] B. Tian, A. X. Liu, C. T. Chong, L. M. Fan, S. Ni, J.-H. Ng, S. Rigopoulos, K. H. Luo, and S. Hochgreb, "Experimental and numerical study on soot formation in laminar diffusion flames of biodiesels and methyl esters," Proceedings of the Combustion Institute (2020).

[52] J. Appel, H. Bockhorn, and M. Frenklach, "Kinetic modeling of soot formation with detailed chemistry and physics: laminar premixed flames of C2 hydrocarbons," Combustion and Flame **121**, 122–136 (2000).

[53] M. Celnik, A. Raj, R. West, R. Petterson, and M. Kraft, "Aromatic site description of soot particles," Combustion and Flame **155**, 161–180 (2008).

[54] D. Hou, C. Lindberg, M. Manuputty, X. You, and M. Kraft, "Modelling soot formation in a benchmark ethylene stagnation flame with a new detailed population balance model," Combustion and Flame **203**, 56–71 (2019).

[55] P. Rodrigues, B. Franzelli, R. Vicquelin, O. Gicquel, and N. Darabiha, "Coupling an les approach and a soot sectional model for the study of sooting turbulent non-premixed flames," Proceeding of the Combustion Institute **190**, 477–499 (Combustion and Flame).

[56] M. Schiener and R. Lindstedt, "Coupling an LES approach and a soot sectional model for the study of sooting turbulent non-premixed flames," Proceeding of the Combustion Institute **37**, 1049–1056 (2019).

[57] A. X. Liu and S. Rigopoulos, "A conservative method for solution of the population balance equation, and application to soot formation," Combustion and Flame **205**, 506–521 (2019).

[58] J. Jeong and M. Choi, "A sectional method for the analysis of growth of polydisperse non-spherical particles undergoing coagulation and coalescence," Journal of Aerosol Science **32**, 565–582 (2001).

[59] A. Veshkini, S. Dworkin, and M. Thomson, "Understanding soot particle size evolution in laminar ethylene/air diffusion flames using novel soot coalescence models," Combustion Theory and Modelling **20** (2016).

[60] B. Sun, S. Rigopoulos, and A. Liu, "Modelling of soot aggregation and sintering with a two-population balance equation model and a conservative finite volume method," Combustion and Flame **in press** (2021).

[61] M. Sander, R. West, M. Celink, and M. Kraft, "A detailed model for the sintering of polydispersed nanoparticle agglomerates," Aerosol Science and Technology **43**, 978–989 (2009).

[62] E. Y. K. Yee, *Numerical Simulation of Soot in Laminar Flames*, Ph.D. thesis, University of Cambridge, UK (2016).

[63] D. O'Sullivan and S. Rigopoulos, "A conservative finite volume method for the population balance equation with aggregation, fragmentation, nucleation and growth," Chemical Engineering Science **263**, 117925 (2022).

[64] M. Köhler, K. Geigle, W. Meier, B. Crosland, K. Thomson, and G. Smallwood, "Sooting turbulent jet flame: characterization and quantitative soot measurements," Applied Physics B: Lasers and Optics **104**, 409–425 (2011).

[65] M. Köhler, I. Boxx, K. Geigle, and W. Meier, "Simultaneous planar measurements of soot structure and velocity fields in a turbulent lifted jet flame at 3 khz," Applied Physics B: Lasers and Optics **103**, 271–279 (2011).

[66] W. Jones and V. Prasad, "Large eddy simulation of the sandia flame series (d-f) using the Eulerian stochastic field method," Combustion and Flame **157**, 1621–1636 (2010).

[67] F. Sewerin and S. Rigopoulos, "An LES-PBE-PDF approach for modeling particle formation in turbulent reacting flows," Physics of Fluids **29**, 105105 (2017).

[68] B. Koren, "A robust upwind discretization method for advection, diffusion and source terms," in *Numerical Methods for Advection-Diffusion Problems: Notes on Numerical Fluid Mechanics and Multidisciplinary Design*, edited by B. Koren and C. Vreugdenhil (Vieweg Verlag, 1993) pp. 117–138.

[69] F. Gao and E. O'Brien, "A large-eddy simulation scheme for turbulent reacting flow," Physics of Fluids: A: Fluid Dynamics **5**, 1282–1284 (1993).

[70] T. Brauner, W. Jones, and A. Marquis, "Les of the cambridge stratified swirl burner using a sub-grid pdf approach," Flow, Turbulent and Combustion **96** (2006).

[71] J. Villermaux and J.-C. Devillon, "Représentation de la redistribution des domaines de ségrégation dans un fluide par un modéle d'interaction phénoménologique," Proceedings of the Second International Symposium on Chemical Reaction Engineering (1972).

[72] C. Dopazo and E. O'Brien, "Functional formulation of nonisothermal turbulent reactive flows," Physics of Fluids **17**, 1968–1975 (1974).

[73] C. Dopazo, "Probability density-function approach for a turbulent axisymmetric heated jet - centerline evolution," Physics of Fluids **18**, 397–404 (1975).

[74] G. Bulat, W. Jones, and A. Marquis, "Large eddy simulation of an industrial gas-turbine combustion chamber using sub-grid pdf method," Proceedings of the Combustion Institute **34**, 3155–3164 (2013).

[75] L. Valiño, "field monte carlo formulation for calculating the probability density function of a single scalar in a turbulent flow," Flow Turbulence and Combustion **60**, 157–172 (1998).

[76] C. Gardiner, *Handbook of Stochastic Methods* (Springer Verlag, 1985).

[77] A. Liu, C. Garcia, F. Sewerin, B. William, and S. Rigopoulos, "Population balance modelling and laser diagnostic validation of soot particle evolution in laminar ethylene diffusion flames," Combustion and Flame **221**, 384–400 (2020).

[78] T. Lu and C. Law, "A directed relation graph method for mechanism reduction," Proceedings of the Combustion Institute **30** (2005).

[79] P. Pepiot-Desjardins and H. Pitsch, "An efficient error-propagation-based reduction method for large chemical kinetic mechanisms," Combustion and Flame **154** (2008).

[80] G. Blanquart and Pitsch, "A joint volume-surface-hydrogen multi-variate model for soot formation," Combustion and Flame **203**, 56–71 (2019).

[81] S. Harris and I. Kennedy, "The coagulation of soot particles with van der waals forces," Combustion Science Technology **59**, 443–454 (1988).

[82] M. Frenklach and H. Wang, "Detailed modeling of soot particle nucleation and growth," International Symposium of the Combustion Institute **23** (1991).

[83] C. J. Dasch, "The decay of soot surface growth reactivity and its importance in total soot formation," Combustion and Flame **61**, 219–225 (1985).

[84] I. T. Woods and B. S. Haynes, "Soot surface growth at active sites," Combustion and Flame **85**, 523–525 (1991).

[85] S. J. Harris and A. M. Weiner, "Chemical kinetics of soot particle growth," Annual Review of Physical Chemistry **36**, 31–52 (1985).

[86] B. S. Haynes and H. G. Wagner, "Soot formation," Progress in Energy and Combustion Science **7**, 229–273 (1981).

[87] A. Veshkini, S. Dworkin, and M. Thomson, "A soot particle surface reactivity model applied to a wide range of laminar ethylene/air flames," Combustion and Flame **161** (2014).

[88] A. Khosousi and S. Dworkin, "Soot surface reactivity during surface growth and oxidation in laminar diffusion flames," Combustion and Flame **162** (2015).

[89] D. Gu, Z. Sun, B. Dally, P. Medwell, Z. Alwahabi, and G. Nathan, "Simultaneous measurements of gas temperature, soot volume fraction and primary particle diameter in a sooting lifted turbulent ethylene/air non-premixed flame," Combustion and Flame **179**, 33–50 (2017).

[90] A. N. Kolmogorov, "Local structure of turbulence in an incompressible fluid at very high reynolds numbers," Dokl. Akad. Nauk SSSR **30**, 299–303 (1941).

[91] A. M. Oboukhov, "Spectral energy distribution in a turbulent flow," Izv. Akad. Nauk. SSSR, Ser. Geogr. Geofiz. **5**, 453–466 (1941).

[92] A. M. Oboukhov, "Structure of temperature field in a turbulent flow," Izv. Akad. Nauk. SSSR, Ser. Geogr. Geofiz. **13**, 58–69 (1949).

[93] G. K. Batchelor, *THe Theory of Homogeneous Turbulence* (Cambridge University Press, 1970).

[94] K. P. Shete, D. J. Boucher, J. J. Riley, and S. M. De Bruyn Kops, "Effect of viscous-convective subrange on passive scalar statistics at high Reynolds number," Physical Review Fluids **7** (2022).

[95] D. Buaria and K. R. Sreenivasan, "Comment on "Effect of viscous-convective subrange on passive scalar statistics at high Reynolds number"," Physical Review Fluids **8** (2023).

[96] D. A. Donzis, K. R. Sreenivasan, and P. K. Yeung, "The Batchelor spectrum for mixing of passive scalars in isotropic turbulence: Submitted for the special issue dedicated to S. B. Pope," Flow, Turbulence and Combustion **85**, 549–566 (2010).

[97] D. A. Donzis and P. K. Yeung, "Resolution effects and scaling in numerical simulations of passive scalar mixing in turbulence," Physica D: Nonlinear Phenomena **239**, 1278–1287 (2010).

[98] J. J. Derksen, "Direct simulations of mixing of liquids with density and viscosity differences," Industrial & Engineering Chemistry Research **51**, 6948–6957 (2012).

[99] D. A. Donzis, K. Aditya, K. R. Sreenivasan, and P. K. Yeung, "The turbulent Schmidt number," Journal of Fluids Engineering, Transactions of the ASME **136**, 060912 (2014).

[100] D. Buaria, M. P. Clay, K. R. Sreenivasan, and P. K. Yeung, "Small-scale isotropy and ramp-cliff structures in scalar turbulence," Physical Review Letters **126**, 034504 (2021).

[101] R. Ranjan and S. Menon, "Two level simulation of Schmidt number effect on passive scalar transport in wall-bounded turbulent flows," Physics of Fluids **33**, 035124 (2021).